



Research paper

Analytical and numerical investigation of second-order infinitesimal mechanism in rigid origami

Kentaro Hayakawa ^{*}, Tomotaka Ohba, Makoto Ohsaki

Department of Architecture and Architectural Engineering, Kyoto University, Kyoto-Daigaku Katsura, Nishikyo, Kyoto, 615-8540, Japan

ARTICLE INFO

Keywords:

Rigid origami
Truss model
Bifurcation path
Second-order infinitesimal mechanism
Finite mechanism

ABSTRACT

This study investigates second-order infinitesimal mechanisms and bifurcation paths of rigid origamis with multiple-degree-of-freedom mechanisms. A truss model, consisting of pin-connected rigid bars, is employed for the infinitesimal mechanism analysis. The conditions for the existence of a second-order infinitesimal mechanism are analytically solved to investigate the combinations of the infinitesimal mechanism modes that are the potential finite mechanisms. Analytical solutions for simple crease patterns show the bifurcation of the deformation paths at the flat state, some disappeared combinations of the mechanism modes in a single path, and the relationship between the nodal displacement and axial force distribution. This comprehensive analysis, using analytical solutions, lays the foundation for understanding bifurcation and finite mechanism of rigid origami, which have not yet been fully explored. These properties are also verified in the finite deformation paths generated by large deformation analysis of a frame model consisting of frame members and hinges, which is suitable for the analysis using general-purpose finite element analysis software. The second-order infinitesimal mechanisms found in this study are confirmed to be able to be extended to the finite mechanisms.

1. Introduction

The kinematics and motion analysis of rigid origami are crucial for engineering folding mechanisms for deployable, retractable, and morphing structures, for example, in the fields of aerospace [1,2], medical equipment [3], robotics [4,5], metamaterials [6,7], and civil and architectural engineering [8,9]. Rigid origami can be classified as a kind of mechanism in which rigid bodies are connected by hinges or pins, and its internal deformation is governed by complicated geometric constraints. The folding motion of a rigid origami, in which the deformation of the structure occurs only at the crease lines, is often referred to as *rigid-folding* motion. In general, the finite deformation of a mechanism is difficult or even impossible to analytically (algebraically) obtain except for mechanisms with simple configurations [10,11] or some special properties [12–14], and a numerical solution is often employed for path tracing that relies on infinitesimal mechanism analysis [15] or structural analysis with elastic deformation [16,17].

In infinitesimal mechanism analysis, displacement of a mechanism is evaluated by the series expansion of its nonlinear geometric constraints; for example, a first-order infinitesimal mechanism is determined from the linear approximation (first-order derivative) of the constraints, and a higher-order infinitesimal mechanism is determined by considering the higher-order terms. The first-order infinitesimal mechanism analysis is widely used for investigating the kinematic properties of rigid origami and folding path tracing [15,18]. When the mechanism has multiple degrees of freedom, the infinitesimal displacement in the space of first-order infinitesimal mechanisms is represented by a linear combination of the multiple infinitesimal mechanism modes. Although the

^{*} Corresponding author.

E-mail addresses: se.hayakawa@archi.kyoto-u.ac.jp (K. Hayakawa), se.oba@archi.kyoto-u.ac.jp (T. Ohba), ohsaki@archi.kyoto-u.ac.jp (M. Ohsaki).

Nomenclature

$(\mathbf{X}', \mathbf{X}'')$	second-order infinitesimal mechanism
$\boldsymbol{\omega} = (\omega_1, \dots, \omega_{N_b})^\top$	assemblage of the axial force density for all the bars
$\delta \mathbf{X}$	displacement of origami vertices calculated from the nodal displacement of the frame model
$\frac{d\mathbf{C}(\mathbf{X})}{d\mathbf{X}} = \left[\frac{\partial c_i}{\partial X_j} \right]$	compatibility matrix
$\frac{d^2\mathbf{C}(\mathbf{X})}{d\mathbf{X}^2} = \left[\frac{\partial^2 c_i}{\partial X_j \partial X_k} \right]$	Hessian tensor of incompatibility vector
J_i	set of indices of the nodes that are the end points of bar i
$\sigma_1, \dots, \sigma_r$	non-zero constants
i, j, k	flexible positive integers within a certain range
l_i	initial length of bar i
m, n	fixed positive integers
N_b	number of bars of a truss model
N_f	number of kinematic indeterminacy
N_n	number of nodes of a truss model
N_s	number of statical indeterminacy
$N_x = 3N_n$	total degrees of freedom for the nodal displacement in a truss model
r	rank of the compatibility matrix
$\mathbf{a} = (a_1, \dots, a_{N_f})^\top$	coefficient vector for the first-order infinitesimal mechanism
\mathbf{A}	coefficient matrix to convert the nodal coordinates of a truss model into the nodal coordinates of the corresponding frame model
\mathbf{A}^+	Moore–Penrose inverse of \mathbf{A}
$\mathbf{a}^{(2)} = (a_1^{(2)}, \dots, a_{N_f}^{(2)})^\top$	coefficient vector for the complementary term of the second-order infinitesimal mechanism
$\mathbf{a}^f = (a_1^f, \dots, a_{N_x}^f)^\top$	coefficient vector of $\mathbf{v}_1, \dots, \mathbf{v}_{N_x}$ to represent $\delta \mathbf{X}$
$\mathbf{a}^o = (a_1^o, \dots, a_{N_x}^o)^\top$	coefficient vector of $\mathbf{v}_1^o, \dots, \mathbf{v}_{N_x}^o$ to represent $\delta \mathbf{X}$
$\mathbf{b}^{(2)} = (b_{N_f+1}^{(2)}, \dots, b_{N_x}^{(2)})^\top$	coefficient vector for the particular term of the second-order infinitesimal mechanism
$\mathbf{C}(\mathbf{X}) = (c_1, \dots, c_{N_b})^\top$	incompatibility vector
\mathbf{T}	coefficient matrix to convert \mathbf{V}^o into \mathbf{V}
$\mathbf{u}_1, \dots, \mathbf{u}_{N_s}$	self-equilibrium force density modes
$\mathbf{u}_{N_s+1}, \dots, \mathbf{u}_{N_b}$	bases of the column space of the compatibility matrix (orthogonal complement of the space of the self-equilibrium force density)
$\mathbf{V} = \left[\mathbf{v}_1 \ \dots \ \mathbf{v}_{N_x} \right]$	matrix of $\mathbf{v}_1, \dots, \mathbf{v}_{N_x}$
$\mathbf{V}^o = \left[\mathbf{v}_1^o \ \dots \ \mathbf{v}_{N_x}^o \right]$	matrix of $\mathbf{v}_1^o, \dots, \mathbf{v}_{N_x}^o$
$\mathbf{v}_1^o, \dots, \mathbf{v}_{N_x}^o$	orthonormal bases of the N_x -dimensional vector space where the first N_f bases correspond to the infinitesimal mechanism modes of a truss model
$\mathbf{v}_1, \dots, \mathbf{v}_{N_f}$	infinitesimal mechanism modes
$\mathbf{V}_f = \left[\mathbf{v}_1 \ \dots \ \mathbf{v}_{N_f} \right]$	matrix of infinitesimal mechanism modes
$\mathbf{V}_r = \left[\mathbf{v}_{N_f+1} \ \dots \ \mathbf{v}_{N_x} \right]$	matrix of $\mathbf{v}_{N_f+1}, \dots, \mathbf{v}_{N_x}$
$\mathbf{v}_{N_f+1}, \dots, \mathbf{v}_{N_x}$	bases of the row space of the compatibility matrix (orthogonal complement of the space of the first-order infinitesimal mechanism)
$\mathbf{X} = (X_1, \dots, X_{N_n})^\top$	assemblage of all the nodal coordinates that vary in the folding process
\mathbf{X}'	first-order infinitesimal mechanism
\mathbf{x}_j''	components of \mathbf{X}'' corresponding to the coordinates of node j
\mathbf{x}_j'	components of \mathbf{X}' corresponding to the coordinates of node j
\mathbf{X}^f	assemblage of all the nodes in the entire frame model
\mathbf{x}_i^f	position vector of node i of a frame model
$\mathbf{x}_j = (x_j, y_j, z_j)^\top$	position vector for node j of a truss model

mechanism modes have infinite combinations, a finite mechanism often exists only in a limited part of them, and further analysis in addition to the first-order infinitesimal mechanism is needed to determine the mechanism modes or their combinations that are potential finite mechanisms. The simplest way to obtain a finite deformation is to carry out a geometrically nonlinear analysis to

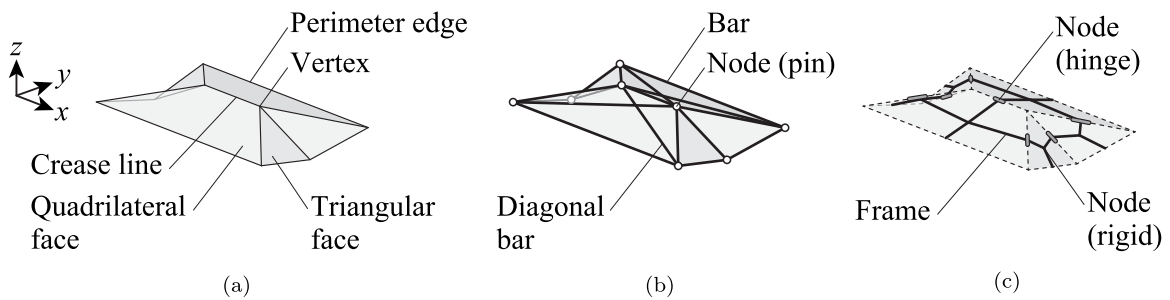


Fig. 1. Examples of rigid origami and its analysis models: (a) configuration of rigid origami with two quadrilateral and four triangular faces, (b) truss model for infinitesimal mechanism analysis, consisting of rigid bars connected by pins, and (c) frame model for large deformation analysis, consisting of rigid frame members rigidly connected on faces and connected by hinges on crease lines.

trace the deformation path [15]. However, it is impractical to cover all possible deformation paths of a multi-degree-of-freedom mechanism by using this approach. Therefore, higher-order infinitesimal mechanism analysis is essential to find a potential finite mechanism. The importance of higher-order infinitesimal mechanisms was pointed out in the 1980s [19,20], and higher-order infinitesimal mechanisms for pin-jointed bar frameworks [21,22] have been extensively investigated. The idea of higher-order infinitesimal mechanisms, especially second-order infinitesimal mechanisms, has also been introduced to the analysis of rigid origami since the 2000s in a different form of equations from bar frameworks [23,24]. Although the existence of a second-order infinitesimal mechanism is generally a necessary but not sufficient condition for the existence of a finite mechanism, Demaine et al. [25] proved the equivalence of the existence of a second-order infinitesimal mechanism and a finite mechanism in special cases, namely, a single interior vertex origami and a flat foldable crease pattern with only degree-4 vertices.

A higher-order infinitesimal mechanism is also important for determining the bifurcation paths at a kinematic bifurcation point where two or more deformation paths intersect, and the degrees of freedom of the mechanism increase. Kumar and Pellegrino [26] presented a method for numerically finding bifurcation paths of a pin-jointed bar structure that has a single-degree-of-freedom mechanism. They investigated a second-order infinitesimal mechanism at the bifurcation point to determine the possible deformation path where the finite mechanism may exist, and they explored the bifurcation paths of several pin-jointed assemblies. Chen et al. [27] applied a second-order infinitesimal mechanism analysis to some specific crease patterns for rigid origami in a flat unfolded state, which is a typical bifurcation point, and counted the number of bifurcation paths. Cai et al. [28] also investigated second-order infinitesimal mechanisms for several crease patterns to numerically list the bifurcation paths. However, the analytical solutions for the existence conditions of a second-order infinitesimal mechanism for a multiple-degree-of-freedom rigid origami have rarely been explored, although the analytical solutions contribute to a deeper and/or wider understanding of the bifurcation at the flat state of a rigid origami. For example, the regions of the coefficients of the infinitesimal mechanism modes where a second-order infinitesimal mechanism can be obtained only when the analytical solutions are available.

Bifurcation of the deformation path has long been studied in the field of structural stability theory rather than in mechanisms. For elastic conservative structural systems, properties of critical points with multiple bifurcation paths, called multiple or coincident bifurcation points, have been extensively investigated [29,30]. It is well known that at most $(3^n - 1)/2$ bifurcation (secondary) paths exist for a structure with n -fold symmetric bifurcation points [31,32]. Magnusson [33] pointed out there may be more than $(3^n - 1)/2$ bifurcation paths for a special case. Ohsaki and Ikeda investigated imperfection sensitivity of a limit point with many bifurcation points [34]. In these studies, the total potential energy consisting of elastic strain energy and work done by the dead load is expanded using the Lyapunov–Schmidt decomposition, and any linear combination of first-order modes satisfies conditions for the second-order mode. Accordingly, for a symmetric system, the bifurcation paths are identified by minimizing the fourth-order term for the energy. However, the rigid origami investigated in this research is usually modeled as a linkage mechanism without elastic stiffness or external loads, and the energy of the structure always vanishes during deformation. Therefore, a question arises whether any combination of first-order infinitesimal modes can satisfy the conditions for a higher-order infinitesimal mode that can lead to bifurcation paths of finite deformation.

In this study, the bifurcation of the kinematic paths of several simple crease patterns, such as the one shown in Fig. 1(a), is investigated by analytically solving the quadratic equations for the existence of second-order infinitesimal mechanisms. The truss model shown in Fig. 1(b) is used for infinitesimal mechanism analysis in which a rigid origami is modeled as a structure consisting of pin-jointed bars. The truss model and its variant, the bar and hinge model, are often used in rigid origami analysis [18,35,36]. It has advantages over, for example, a folding angle model [23,24] and the screw theory [37] in that the geometric and mechanical interpretation of the variables, the compatibility conditions, and the internal forces associated with the compatibility conditions are more straightforward. A first-order infinitesimal mechanism for the truss model is represented by a linear combination of the infinitesimal mechanism modes, and the quadratic equations over the coefficients of the modes are formulated for the existence of a second-order infinitesimal mechanism. In this study, the infinitesimal mechanism analysis is carried out for some simple crease patterns in which the equations for determining the first- and second-order infinitesimal mechanisms can be algebraically solved. In addition, finite deformation paths are generated by large deformation analysis of the frame model shown in Fig. 1(c), which consists of frame members and hinges and is suitable for analysis using general-purpose finite element analysis software [38,39]. By using

the frame model, we can easily assign small rotation stiffness to the hinges, and this stiffness stabilizes the convergence process at each step in the large deformation analysis. The obtained large deformation paths are compared to the results of the infinitesimal mechanism analysis. This study makes the following key contributions for rigid origamis with some simple crease patterns:

- Systems of quadratic equations for the existence of second-order infinitesimal mechanisms are algebraically solved for the coefficients of the infinitesimal mechanism modes,
- The bifurcation paths are counted and listed based on the solutions to the quadratic equations over the coefficients of the infinitesimal mechanism modes, that have not been fully explored based on these analytical solutions in the previous studies especially for multiple-degree-of-freedom rigid origamis,
- Some combinations of the infinitesimal mechanism modes are shown to disappear when the second-order infinitesimal mechanisms are considered, and
- The mechanism modes corresponding to the local out-of-plane deformation of the truss model for quadrilateral faces are proved to vanish when the second-order infinitesimal mechanism is incorporated. This second-order rigidity of a quadrilateral face significantly simplifies the construction of the truss model; neither the planarity condition [18] nor a three-dimensional bar assembly [36] is necessary.

Through the above contributions, the qualitative insight into bifurcation and finite mechanism of rigid origami are provided and the groundwork is laid for the analysis of more complex rigid origami.

The structure of the rest of this paper is as follows. Section 2 provides the preliminary results of the infinitesimal mechanism analysis of a truss model. The equations governing the first- and second-order infinitesimal mechanisms are shown in their general form. The solutions for the conditions for the first- and second-order infinitesimal mechanisms are provided in Section 3; these are represented as combinations of the infinitesimal mechanism modes and their orthogonal complement modes. In Section 4, the second-order rigidity of a planar quadrilateral face is proved in the case where the bars of a truss model are placed along all the sides and diagonals. The procedure for comparison between the results of the infinitesimal mechanism analysis of the truss model and the large deformation analysis of the frame model is shown in Section 5. Section 6 shows the analyses for crease patterns based on Miura-ori, waterbomb tessellations, and flasher. Concluding remarks are provided in Section 7 to summarize the analysis and discuss the potential extension and limitations of the proposed procedure.

2. Preliminary results

In this article, the rigid-folding mechanisms for rigid origami structures are investigated with a truss model, which consists of rigid bars connected by pins at the vertices. This section provides the essential definitions and equations of the first- and second-order rigidity and infinitesimal mechanism for the truss model, which have been well studied for bar frameworks [19,21,26], tensegrities [40], partially rigid frames [41], and rigid origamis [25,42]. Formulations similar to those in this section can also be found in Refs. [27,28].

2.1. Rigidity and infinitesimal mechanism for truss model

In the truss model used in this study, nodes are placed at the vertices, and bars are placed along the crease lines, the perimeter edges, and the diagonals of faces as shown in Fig. 1(b). Let N_n and N_b denote the number of nodes and bars, respectively, of a truss model. Although a rigid origami with only triangular and quadrilateral faces is investigated in this paper, it is expected that the presented methodology can be easily extended to a rigid origami containing faces with more than four sides. The position vector for node j ($j = 1, \dots, N_n$) is denoted by $\mathbf{x}_j = (x_j, y_j, z_j)^T \in \mathbb{R}^3$. In addition, let \mathcal{J}_i denote the set of indices of the nodes that are the end points of bar i ($i = 1, \dots, N_b$). When nodes j and k ($j, k \in \mathcal{J}_i$) are the end points of bar i ($i = 1, \dots, N_b$) whose initial length is $l_i \in \mathbb{R}$, the compatibility equation over the position vectors of these nodes is formulated as

$$c_i = \frac{1}{2} (\|\mathbf{x}_j - \mathbf{x}_k\|^2 - l_i^2) = 0 \quad (i = 1, \dots, N_b; j, k \in \mathcal{J}_i) \quad (1)$$

so that the length of bar i does not change when \mathbf{x}_j and \mathbf{x}_k change. In the following formulations, the boundary conditions are not incorporated, and the six degrees of freedom of the rigid-body motion for the entire truss model are also included in the infinitesimal mechanism analysis. Defining the total degrees of freedom $N_x = 3N_n$, all the nodal coordinates that vary in the folding process are assembled into a column vector $\mathbf{X} = (\mathbf{x}_1^T, \dots, \mathbf{x}_{N_n}^T)^T \in \mathbb{R}^{N_x}$. The j th component of \mathbf{X} is denoted by X_j ($j = 1, \dots, N_x$). Then, c_i ($i = 1, \dots, N_b$) for all the bars are assembled into an *incompatibility vector* $\mathbf{C}(\mathbf{X}) = (c_1, \dots, c_{N_b})^T \in \mathbb{R}^{N_b}$, which is regarded as a function of \mathbf{X} . Eq. (1) for the entire truss model is written in a vector form as follows:

$$\mathbf{C}(\mathbf{X}) = \mathbf{0}. \quad (2)$$

The truss model has the *first-order infinitesimal mechanism* $\mathbf{X}' \in \mathbb{R}^{N_x}$ at the nodal position \mathbf{X} if \mathbf{X}' satisfies

$$\frac{d\mathbf{C}(\mathbf{X})}{d\mathbf{X}} \mathbf{X}' = \mathbf{0}, \quad (3)$$

where $d\mathbf{C}(\mathbf{X})/d\mathbf{X} \in \mathbb{R}^{N_b \times N_x}$ is the *compatibility matrix* whose (i, j) component is $\partial c_i / \partial X_j$ ($i = 1, \dots, N_b; j = 1, \dots, N_x$). The first-order infinitesimal mechanism \mathbf{X}' is *trivial* if its components $x'_j \in \mathbb{R}^3$ ($j = 1, \dots, N_n$) corresponding to the coordinates of node j are transformed from \mathbf{x}_j by rigid-body translation and rotation as

$$\mathbf{x}'_j = \mathbf{S}\mathbf{x}_j + \mathbf{u} \quad (4)$$

for all $j = 1, \dots, N_n$, where \mathbf{S} and \mathbf{u} are a 3×3 skew-symmetric matrix and a three-dimensional vector, respectively, which are common to all the nodes. A trivial first-order infinitesimal mechanism represents the rigid-body motion of the entire truss model in which the model moves without changing its entire shape. If the truss has only trivial first-order infinitesimal mechanisms, it is *first-order rigid*. In the following, the argument \mathbf{X} will be omitted unless necessary, and the infinitesimal mechanism is evaluated at the nodal position \mathbf{X} . The derivatives of c_i ($i = 1, \dots, N_b$) with respect to x_j, y_j , and z_j ($j = 1, \dots, N_n$), which are the components of the compatibility matrix, are calculated as follows:

$$\left(\frac{\partial c_i}{\partial x_j}, \frac{\partial c_i}{\partial y_j}, \frac{\partial c_i}{\partial z_j} \right)^T = \begin{cases} \mathbf{x}_j - \mathbf{x}_k & (\text{If } j, k \in \mathcal{J}_i; j \neq k) \\ \mathbf{0} & (\text{otherwise}). \end{cases} \quad (5)$$

Note that Eq. (3) is obtained by differentiating Eq. (2) once, and \mathbf{X}' can be regarded as the infinitesimal nodal displacement. Then, Eq. (3) for bar i is written as

$$(\mathbf{x}_j - \mathbf{x}_k)^T (\mathbf{x}'_j - \mathbf{x}'_k) = 0 \quad (i = 1, \dots, N_b; j, k \in \mathcal{J}_i). \quad (6)$$

Furthermore, the truss model has the *second-order infinitesimal mechanism* $(\mathbf{X}', \mathbf{X}'') \in (\mathbb{R}^{N_x}, \mathbb{R}^{N_x})$ at the nodal position \mathbf{X} if \mathbf{X}' and \mathbf{X}'' satisfy

$$\begin{cases} \frac{d\mathbf{C}}{d\mathbf{X}} \mathbf{X}' = \mathbf{0} \\ \frac{d\mathbf{C}}{d\mathbf{X}} \mathbf{X}'' + \left[\frac{d^2\mathbf{C}}{d\mathbf{X}^2} \mathbf{X}' \right] \mathbf{X}' = \mathbf{0} \end{cases} \quad (\mathbf{X}' \text{ is non-trivial}), \quad (7)$$

where $d^2\mathbf{C}/d\mathbf{X}^2 \in \mathbb{R}^{N_b \times N_x \times N_x}$ is the order-3 Hessian tensor [42] of the incompatibility vector \mathbf{C} whose (i, j, k) component is $\partial^2 c_i / \partial X_j \partial X_k$ ($i = 1, \dots, N_b; j, k = 1, \dots, N_x$). Otherwise, the truss model is *second-order rigid*. The second-order derivatives of c_i ($i = 1, \dots, N_b$) with respect to the nodal coordinates are calculated as follows:

$$\begin{aligned} \frac{\partial^2 c_i}{\partial x_j^2} &= \frac{\partial^2 c_i}{\partial y_j^2} = \frac{\partial^2 c_i}{\partial z_j^2} = \begin{cases} 1 & (\text{If } j \in \mathcal{J}_i) \\ 0 & (\text{otherwise}), \end{cases} \\ \frac{\partial^2 c_i}{\partial x_j \partial x_k} &= \frac{\partial^2 c_i}{\partial y_j \partial y_k} = \frac{\partial^2 c_i}{\partial z_j \partial z_k} = \begin{cases} -1 & (\text{If } j, k \in \mathcal{J}_i; j \neq k) \\ 0 & (\text{otherwise}), \end{cases} \\ \frac{\partial^2 c_i}{\partial x_j \partial y_j} &= \frac{\partial^2 c_i}{\partial x_j \partial z_j} = \frac{\partial^2 c_i}{\partial y_j \partial z_j} = \frac{\partial^2 c_i}{\partial x_j \partial y_k} = \frac{\partial^2 c_i}{\partial x_j \partial z_k} = \frac{\partial^2 c_i}{\partial y_j \partial z_k} = 0 \quad (j \neq k). \end{aligned} \quad (8)$$

Note that Eq. (7) is obtained by differentiating Eq. (2) twice. Let $\mathbf{x}''_j \in \mathbb{R}^3$ ($j = 1, \dots, N_x$) denote the vector consisting of the components of the second-order infinitesimal mechanism \mathbf{X}'' that relate to node j . Then, the second equation in Eq. (7) for bar i is written as

$$(\mathbf{x}_j - \mathbf{x}_k)^T (\mathbf{x}''_j - \mathbf{x}''_k) + (\mathbf{x}'_j - \mathbf{x}'_k)^T (\mathbf{x}'_j - \mathbf{x}'_k) = 0 \quad (i = 1, \dots, N_b; j, k \in \mathcal{J}_i). \quad (9)$$

The third- and higher-order mechanisms can also be derived by further differentiating Eq. (2) as shown in Ref. [41]. Because the third- and higher-order derivatives of \mathbf{C} with respect to \mathbf{X} are equal to zero, only $d\mathbf{C}/d\mathbf{X}$ and $d^2\mathbf{C}/d\mathbf{X}^2$ appear in the equations determining the higher-order infinitesimal mechanisms in a manner similar to that in Eqs. (3) and (7).

2.2. Self-equilibrium force and second-order infinitesimal mechanism

This subsection shows the relationship between the self-equilibrium force and the second-order infinitesimal mechanism for the truss model. When we define ω_i as the axial force density (the axial force divided by the bar length) of bar i ($i = 1, \dots, N_b$), the equilibrium equation at node j ($j = 1, \dots, N_n$) without an external load is formulated as

$$\sum_{\substack{i \in I_j \\ k \in \mathcal{J}_i \\ k \neq j}} \omega_i (\mathbf{x}_j - \mathbf{x}_k) = \mathbf{0}, \quad (10)$$

where I_j is the set of indices of the bars connected to node j . When ω_i for all the bars is assembled into a vector $\boldsymbol{\omega} = (\omega_1, \dots, \omega_{N_b})^T \in \mathbb{R}^{N_b}$, the equilibrium Eqs. (10) for all the nodes can be written in vector form as follows:

$$\boldsymbol{\omega}^T \frac{d\mathbf{C}}{d\mathbf{X}} = \mathbf{0}^T. \quad (11)$$

Here, $\boldsymbol{\omega}$ satisfying Eq. (11) is referred to as the *self-equilibrium force density*. We can see from Eqs. (3) and (11) that the first-order infinitesimal mechanism \mathbf{X}' and the self-equilibrium force density $\boldsymbol{\omega}$ are in the null space and the left null space of $d\mathbf{C}/d\mathbf{X}$, respectively [43]. The dimensions of the null space and the left null space, which are the number of linearly independent bases for these vector spaces, are referred to as the *number of kinematic indeterminacy* and the *number of statical indeterminacy*, respectively. The numbers of kinematic and statical indeterminacies, denoted by N_f and N_s , respectively, are calculated as follows:

$$N_f = N_x - \text{rank} \left(\frac{d\mathbf{C}}{d\mathbf{X}} \right), \quad (12)$$

$$N_s = N_b - \text{rank} \left(\frac{dC}{dX} \right). \quad (13)$$

Note that N_f includes the six degrees of freedom of the rigid-body motion; that is, the degrees of freedom of the rigid-folding motion are $N_f - 6$.

Next, the condition for the existence of the second-order infinitesimal mechanism is shown. In the rest of this subsection, we assume that $N_f \geq 7$. According to Eq. (7), a second-order infinitesimal mechanism X'' exists with the first-order infinitesimal mechanism X' satisfying Eq. (3) if and only if there exists a solution to the following linear system:

$$\frac{dC}{dX} X'' = - \left[\frac{d^2C}{dX^2} X' \right] X'. \quad (14)$$

This implies that the right-hand side of Eq. (14) needs to lie in the column space of dC/dX , which is orthogonal to the left null space of dC/dX . On the other hand, the entire space of the self-equilibrium force density ω agrees with the entire left null space of dC/dX . Therefore, a solution to Eq. (14) exists if and only if all the possible self-equilibrium force densities ω satisfy the following equation:

$$\omega^T \left[\frac{d^2C}{dX^2} X' \right] X' = X'^T \left[\omega^T \frac{d^2C}{dX^2} \right] X' = 0, \quad (15)$$

where $[\omega^T d^2C/dX^2]$ is the $N_x \times N_x$ matrix calculated as

$$\left[\omega^T \frac{d^2C}{dX^2} \right] = \sum_{i=1}^{N_b} \omega_i \begin{bmatrix} \frac{\partial^2 c_i}{\partial X_1^2} & \cdots & \frac{\partial^2 c_i}{\partial X_1 \partial X_{N_x}} \\ \vdots & \ddots & \vdots \\ \frac{\partial^2 c_i}{\partial X_1 \partial X_{N_x}} & \cdots & \frac{\partial^2 c_i}{\partial X_{N_x}^2} \end{bmatrix}.$$

Contrarily, if there exists a self-equilibrium force density ω that corresponds to the non-vanishing quadratic form $X'^T [\omega^T d^2C/dX^2] X'$ with non-trivial X' , the truss model is second-order rigid. Note that $[\omega^T d^2C/dX^2]$ is identical to the geometrical stiffness matrix for the pin-jointed structures shown in Eq. (29) of Ref. [44].

3. Derivation of infinitesimal mechanisms

In this section, the first- and second-order infinitesimal mechanisms are derived using the bases of the vector spaces defined by the compatibility matrix.

3.1. First-order infinitesimal mechanism

A first-order infinitesimal mechanism is represented by a linear combination of N_f bases of the null space of dC/dX , which are referred to as the *infinitesimal mechanism modes*, and these bases are denoted by the linearly independent vectors $\mathbf{v}_1, \dots, \mathbf{v}_{N_f} \in \mathbb{R}^{N_x}$, which include the six rigid-body motions. Then, a first-order infinitesimal mechanism X' satisfying Eq. (3) can be written by using a coefficient vector $\mathbf{a} = (a_1 \dots, a_{N_f})^T \in \mathbb{R}^{N_f}$ and the matrix $\mathbf{V}_f = [\mathbf{v}_1 \dots \mathbf{v}_{N_f}] \in \mathbb{R}^{N_x \times N_f}$ as follows:

$$X' = a_1 \mathbf{v}_1 + \dots + a_{N_f} \mathbf{v}_{N_f} = \mathbf{V}_f \mathbf{a}. \quad (16)$$

The following discussion assumes that $\mathbf{v}_{N_f-5}, \dots, \mathbf{v}_{N_f}$ represent the rigid-body motions and are orthogonal to the remaining bases $\mathbf{v}_1, \dots, \mathbf{v}_{N_f-6}$. We refer to $\mathbf{v}_1, \dots, \mathbf{v}_{N_f-6}$ as the *non-trivial* infinitesimal mechanism modes, which represent the rigid-folding modes.

3.2. Second-order infinitesimal mechanism

We first show the condition for the existence of a second-order infinitesimal mechanism in the direction of the first-order infinitesimal mechanism written in the form of Eq. (16). When $N_s \geq 1$, linearly independent vectors $\mathbf{u}_1, \dots, \mathbf{u}_{N_s} \in \mathbb{R}^{N_b}$ denote the bases of the left null space of dC/dX , which are referred to as the *self-equilibrium force density modes*. Then, an arbitrary self-equilibrium force density ω satisfying Eq. (11) can be expressed as a linear combination of $\mathbf{u}_1, \dots, \mathbf{u}_{N_s}$. Therefore, the condition (15) for the existence of a second-order infinitesimal mechanism is equivalent to the following condition for all $i = 1, \dots, N_s$:

$$\mathbf{a}^T \mathbf{V}_f^T \left[\mathbf{u}_i^T \frac{d^2C}{dX^2} \right] \mathbf{V}_f \mathbf{a} = 0 \quad (i = 1, \dots, N_s). \quad (17)$$

Next, a second-order infinitesimal mechanism is derived under condition (17) with a non-zero \mathbf{a} . Although the second-order infinitesimal mechanisms are not derived in the examples in this paper, their formulations are shown for the completeness of the second-order infinitesimal mechanism analysis. The bases of the row space of dC/dX are denoted by the linearly independent vectors $\mathbf{v}_{N_f+1}, \dots, \mathbf{v}_{N_x} \in \mathbb{R}^{N_x}$, and they are assembled into a matrix $\mathbf{V}_r = [\mathbf{v}_{N_f+1} \dots \mathbf{v}_{N_x}] \in \mathbb{R}^{N_x \times N_x - N_f}$. Then, we can write a second-order

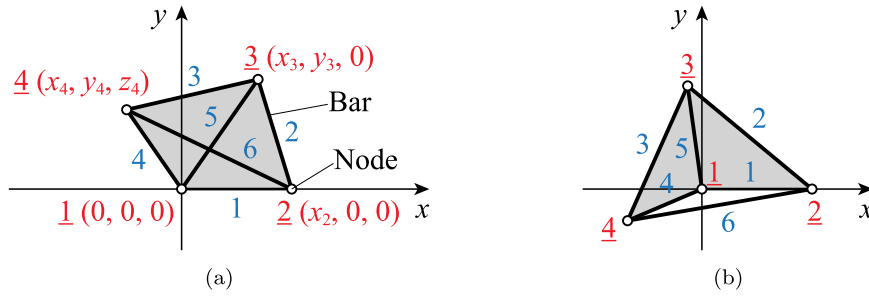


Fig. 2. Planar quadrilateral face and its node indices (red with underlining) and bar indices (blue): (a) convex face, (b) concave face. (For interpretation of the references to color in this figure legend, the reader is referred to the web version of this article.)

infinitesimal mechanism \mathbf{X}'' by using coefficient vectors $\mathbf{a}^{(2)} = (a_1^{(2)} \dots, a_{N_f}^{(2)})^T \in \mathbb{R}^{N_f}$ and $\mathbf{b}^{(2)} = (b_{N_f+1}^{(2)} \dots, b_{N_x}^{(2)})^T \in \mathbb{R}^{(N_x - N_f)}$ as follows:

$$\mathbf{X}'' = a_1^{(2)} \mathbf{v}_1 + \dots + a_{N_f}^{(2)} \mathbf{v}_{N_f} + b_{N_f+1}^{(2)} \mathbf{v}_{N_f+1} + \dots + b_{N_x}^{(2)} \mathbf{v}_{N_x} = \mathbf{V}_f \mathbf{a}^{(2)} + \mathbf{V}_r \mathbf{b}^{(2)}. \tag{18}$$

Note that the vectors $\mathbf{v}_1, \dots, \mathbf{v}_{N_x}$ form the linearly independent bases of the N_x -dimensional space. In addition, let linearly independent vectors $\mathbf{u}_{N_s+1}, \dots, \mathbf{u}_{N_b} \in \mathbb{R}^{N_b}$ denote the bases of the column space of $d\mathbf{C}/d\mathbf{X}$. Here, $\mathbf{v}_{N_f+1}, \dots, \mathbf{v}_{N_x}$ and $\mathbf{u}_{N_s+1}, \dots, \mathbf{u}_{N_b}$ are determined so that they form orthonormal bases and satisfy the following relations:

$$\mathbf{u}_i^T \mathbf{u}_j = \begin{cases} 1 & (i = j) \\ 0 & (i \neq j) \end{cases} \quad (i, j = N_s + 1, \dots, N_b), \tag{19}$$

$$\frac{d\mathbf{C}}{d\mathbf{X}} \mathbf{v}_{N_f+i} = \sigma_i \mathbf{u}_{N_s+i} \quad (i = 1, \dots, r), \tag{20}$$

where $r = N_x - N_f = N_b - N_s = \text{rank}(d\mathbf{C}/d\mathbf{X})$ and $\sigma_i \in \mathbb{R} \ (i = 1, \dots, r)$ is a non-zero constant.

Remark 1. Vectors $\mathbf{v}_i \ (i = 1, \dots, N_x)$ and $\mathbf{u}_i \ (i = 1, \dots, N_b)$ may be derived by the singular value decomposition of $d\mathbf{C}/d\mathbf{X}$ so that \mathbf{v}_i and \mathbf{u}_i correspond to the right and left singular vectors, respectively [41,43]. In this case, $\sigma_i \ (i = 1, \dots, r)$ in Eq. (20) is a non-zero singular value of $d\mathbf{C}/d\mathbf{X}$.

The following equation is obtained by substituting Eqs. (18) and (20) into Eq. (14):

$$\frac{d\mathbf{C}}{d\mathbf{X}} \mathbf{V}_r \mathbf{b} = b_{N_f+1}^{(2)} \sigma_1 \mathbf{u}_{N_s+1} + \dots + b_{N_x}^{(2)} \sigma_r \mathbf{u}_{N_b} = - \left[\frac{d^2 \mathbf{C}}{d\mathbf{X}^2} \mathbf{X}' \right] \mathbf{X}'. \tag{21}$$

According to Eq. (19), $b_{N_f+i}^{(2)} \ (i = 1, \dots, r)$ is determined from Eq. (21) as follows:

$$\begin{aligned} b_{N_f+i}^{(2)} &= - \frac{1}{\sigma_i} \mathbf{u}_{N_s+i}^T \left[\frac{d^2 \mathbf{C}}{d\mathbf{X}^2} \mathbf{X}' \right] \mathbf{X}' \\ &= - \frac{1}{\sigma_i} \mathbf{X}'^T \left[\mathbf{u}_{N_s+i}^T \frac{d^2 \mathbf{C}}{d\mathbf{X}^2} \right] \mathbf{X}' \quad (i = 1, \dots, r). \\ &= - \frac{1}{\sigma_i} \mathbf{a}^T \mathbf{V}_f^T \left[\mathbf{u}_{N_s+i}^T \frac{d^2 \mathbf{C}}{d\mathbf{X}^2} \right] \mathbf{V}_f \mathbf{a} \end{aligned} \tag{22}$$

$\mathbf{a}^{(2)}$ can be an arbitrary real vector if the existence conditions for the third- and higher-order mechanisms are not considered. Note that $\mathbf{a}^{(2)}$ is often assumed to be zero because the existence conditions for the higher-order mechanisms can be satisfied with $\mathbf{a}^{(2)} = \mathbf{0}$ [41].

Remark 2. An n -th-order infinitesimal mechanism $\mathbf{X}^{(n)}$ ($n \geq 1$) can be written in the form

$$\mathbf{X}^{(n)} = \mathbf{V}_f \mathbf{a}^{(n)} + \mathbf{V}_r \mathbf{b}^{(n)}, \tag{23}$$

where $\mathbf{b}^{(n)} \in \mathbb{R}^{N_x - N_f}$ is completely determined from the lower-order infinitesimal mechanisms [see Eq. (22) for $n = 2$], while $\mathbf{a}^{(n)} \in \mathbb{R}^{N_f}$ is constrained by the existence conditions for the $(n + 1)$ th and higher-order mechanisms.

4. Second-order rigidity of quadrilateral face

Here we show that, when the bars of a truss model of a planar quadrilateral face are placed along all the sides and diagonals that have non-zero length, the truss model corresponding to this single quadrilateral face is second-order rigid. As shown in Fig. 2, both convex and concave faces are considered, and we also consider the case where three of four vertices are on the same line.

The second-order rigidity of a quadrilateral face ensures that neither the planarity condition [18] nor the three-dimensional bar assembly [36] is necessary to guarantee out-of-plane rigidity, and we only need to arrange the bars along the edges and the diagonals of faces. This significantly simplifies the construction and configuration of the truss model.

Without loss of generality, we can assume the initial position and the displacement boundary condition of a planar quadrilateral face so that nodes 1, 2, and 3 are fixed at the origin, on the positive part of the x -axis, and on the xy -plane, respectively, as shown in Fig. 2. Nodes 1 – 4 are arranged in a counterclockwise fashion and nodes 1, 2, and 3 are not colinear. These boundary conditions can be incorporated by simply omitting the corresponding components from \mathbf{X} , $d\mathbf{C}/d\mathbf{X}$, and $d^2\mathbf{C}/d\mathbf{X}^2$. Because the scale of the face does not affect the rigidity, it can also be assumed that the initial length of the bar connecting nodes 1 and 2 is 1. Bars 1 – 6 are also arranged as shown in Fig. 2. Then, the second-order rigidity of the quadrilateral face with the nodal position vector $\mathbf{X} = (x_2, x_3, y_3, x_4, y_4, z_4)^T = (1, x_3, y_3, x_4, y_4, 0)^T \in \mathbb{R}^6$ ($y_3 \neq 0$) is investigated. Here, the x -coordinates of nodes 2, 3, and 4; the y -coordinates of nodes 3 and 4; and the z -coordinate of node 4 are allowed to vary. The compatibility matrix is calculated as

$$\frac{d\mathbf{C}}{d\mathbf{X}} = \begin{bmatrix} 1 & 0 & 0 & 0 & 0 & 0 \\ 1-x_3 & x_3-1 & y_3 & 0 & 0 & 0 \\ 0 & x_3-x_4 & y_3-y_4 & x_4-x_3 & y_4-y_3 & 0 \\ 0 & 0 & 0 & x_4 & y_4 & 0 \\ 0 & x_3 & y_3 & 0 & 0 & 0 \\ 1-x_4 & 0 & 0 & x_4-1 & y_4 & 0 \end{bmatrix} \in \mathbb{R}^{6 \times 6}. \quad (24)$$

Let $\mathbf{X}' = (x'_2, x'_3, y'_3, x'_4, y'_4, z'_4)^T \in \mathbb{R}^6$ denote a first-order infinitesimal mechanism. The components of \mathbf{X}' can be determined from the following equation when $y_3 \neq 0$:

$$\frac{d\mathbf{C}}{d\mathbf{X}} \mathbf{X}' = \mathbf{0} \Leftrightarrow \begin{cases} x'_2 = 0 \\ (1-x_3)(x'_2-x'_3) + y_3 y'_3 = 0 \\ (x_3-x_4)(x'_3-x'_4) + (y_3-y_4)(y'_3-y'_4) = 0 \\ x_4 x'_4 + y_4 y'_4 = 0 \\ x_3 x'_3 + y_3 y'_3 = 0 \\ (1-x_4)(x'_2-x'_4) + y_4 y'_4 = 0 \end{cases} \quad (25)$$

$$\Leftrightarrow x'_2 = x'_3 = y'_3 = x'_4 = y'_4 = 0.$$

Therefore, the first-order infinitesimal mechanism for the truss model of a single quadrilateral face can be written as $\mathbf{X}' = (0, 0, 0, 0, 0, z'_4)^T$, where z'_4 is a non-zero arbitrary real number. In contrast, let $\boldsymbol{\omega} = (\omega_1, \omega_2, \omega_3, \omega_4, \omega_5, \omega_6)^T \in \mathbb{R}^6$ denote a self-equilibrium force density vector. Because x_4 and y_4 cannot be simultaneously equal to zero and $y_3 \neq 0$, the components of $\boldsymbol{\omega}$ can be obtained using an arbitrary real number $\alpha \in \mathbb{R}$ as follows:

$$\boldsymbol{\omega}^T \frac{d\mathbf{C}}{d\mathbf{X}} = \mathbf{0}^T \Leftrightarrow \begin{cases} \omega_1 + (1-x_3)\omega_2 + (1-x_4)\omega_6 = 0 \\ (x_3-1)\omega_2 + (x_3-x_4)\omega_3 + x_3\omega_5 = 0 \\ y_3\omega_2 + (y_3-y_4)\omega_3 + y_3\omega_5 = 0 \\ (x_4-x_3)\omega_3 + x_4\omega_4 + (x_4-1)\omega_6 = 0 \\ (y_4-y_3)\omega_3 + y_4\omega_4 + y_4\omega_6 = 0 \end{cases} \quad (26)$$

$$\Leftrightarrow \boldsymbol{\omega} = \alpha \begin{pmatrix} (x_3 y_4 - x_4 y_3) [(x_3 - 1) y_4 - (x_4 - 1) y_3] \\ y_4 (x_3 y_4 - x_4 y_3) \\ y_3 y_4 \\ y_3 [(x_3 - 1) y_4 - (x_4 - 1) y_3] \\ -y_4 [(x_3 - 1) y_4 - (x_4 - 1) y_3] \\ -y_3 (x_3 y_4 - x_4 y_3) \end{pmatrix}.$$

The quadratic form in Eq. (15) with the first-order infinitesimal mechanism \mathbf{X}' determined by Eq. (25) and the self-equilibrium force density $\boldsymbol{\omega}$ in Eq. (26) is calculated as

$$\begin{aligned} & \mathbf{X}'^T \left[\boldsymbol{\omega}^T \frac{d^2\mathbf{C}}{d\mathbf{X}^2} \right] \mathbf{X}' \\ &= (\omega_1 + \omega_2 + \omega_6) (x'_2)^2 + (\omega_2 + \omega_3 + \omega_5) (x'_3)^2 + (\omega_2 + \omega_3 + \omega_5) (y'_3)^2 \\ & \quad + (\omega_3 + \omega_4 + \omega_6) (x'_4)^2 + (\omega_3 + \omega_4 + \omega_6) (y'_4)^2 + (\omega_3 + \omega_4 + \omega_6) (z'_4)^2 \\ & \quad - 2\omega_2 x'_2 x'_3 - 2\omega_6 x'_2 x'_4 - 2\omega_3 x'_3 x'_4 - 2\omega_3 y'_3 y'_4 \\ &= (\alpha y_3 z'_4)^2. \end{aligned} \quad (27)$$

According to condition (15) for the existence of the second-order infinitesimal mechanism, if the truss model considered here has a second-order infinitesimal mechanism, the following equation needs to hold for an arbitrary α from Eq. (27):

$$\alpha y_3 z'_4 = 0. \quad (28)$$

Translation and rotation of a single node on a face is fixed to constrain the rigid body motion.

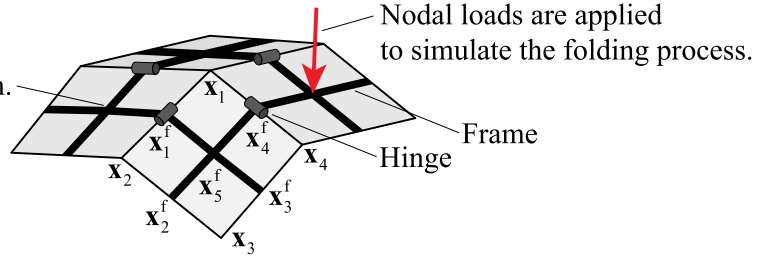


Fig. 3. Structure of the frame model for large deformation analysis using general-purpose finite element analysis software. An n -gonal face is modeled by n frame members rigidly connected on the face and hinge-connected on crease lines.

Because $y_3 \neq 0$ and $z'_4 \neq 0$, there is no solution to Eq. (28). Therefore, the truss model of a single quadrilateral face is second-order rigid.

5. Comparison between infinitesimal mechanism and large deformation analysis

To evaluate the results of the infinitesimal mechanism analysis described above, a large deformation analysis is carried out, and the obtained folding path is investigated with respect to the transition of the coefficients of the infinitesimal mechanism modes. In this study, for the large deformation analysis, the frame model [38,39] consisting of frame members and hinges is used in the general-purpose finite element analysis software Abaqus 2022 [45]. Fig. 3 shows the configuration of a frame model in which an m -gonal face ($m \geq 3$) is modeled by m frame members rigidly connected on the face and connected by hinges on the crease lines. In the large deformation analysis using Abaqus, sufficiently large stiffness is assigned to the frame members to approximately simulate the rigid-folding path. To generate various folding paths, nodal loads are randomly applied to the frame model, and the translation and rotation of the node on a single face is fixed to avoid rigid-body motion. The frame model is used instead of the truss model for the following reasons:

- The rigid-body motion of a rigid origami can be constrained more easily than it can be for a truss model by simply fixing the translation and rotation of the node on a single face.
- The convergence process at each step in the large deformation path analysis can be easily stabilized by assigning a small rotation stiffness to the hinges.
- Out-of-plane stiffness (first-order rigidity) is guaranteed even for the faces with more than three edges in the frame model, which contributes to a stabler analysis process.

Although the nodes of the frame model are not located at the origami vertices, the vertex positions or displacements can be obtained through the simple calculation described below. Consider an m -gonal face ($m \geq 3$) whose vertices are indexed from 1 to m counterclockwise (see Fig. 3 for the quadrilateral face). We place nodes 1, ..., m of the frame model at the center points of the edges, and the position vector $\mathbf{x}_i^f \in \mathbb{R}^3$ ($i = 1, \dots, m$) of node i is determined as follows:

$$\mathbf{x}_i^f = \frac{\mathbf{x}_i + \mathbf{x}_{i+1}}{2} \quad (i = 1, \dots, m; \mathbf{x}_{m+1} = \mathbf{x}_1), \quad (29)$$

where $\mathbf{x}_i \in \mathbb{R}^3$ is the position vector of node i . Furthermore, the position vector $\mathbf{x}_{m+1}^f \in \mathbb{R}^3$ of node $m+1$ placed at the center of the face is determined as

$$\mathbf{x}_{m+1}^f = \frac{1}{m} \sum_{i=1}^m \mathbf{x}_i. \quad (30)$$

When the position vectors of all the nodes in the entire frame model are assembled into a vector $\mathbf{X}^f \in \mathbb{R}^{3N_n^f}$ where N_n^f is the number of nodes, the relationship between the nodal position of the frame model and the vertex position of the origami, which is equivalent to the nodal position of the truss model, can be written in the following form from Eqs. (29) and (30):

$$\mathbf{X}^f = \mathbf{A}\mathbf{X}, \quad (31)$$

where \mathbf{A} is a $3N_n^f \times 3N_n$ matrix. According to Eq. (31), we can obtain the vertex position \mathbf{X} from the nodal position \mathbf{X}^f of the frame model, which is obtained from the large deformation analysis, as follows:

$$\mathbf{X} = \mathbf{A}^+ \mathbf{X}^f, \quad (32)$$

where $\mathbf{A}^+ \in \mathbb{R}^{3N_n \times 3N_n^f}$ is the Moore–Penrose inverse of \mathbf{A} [43].

The vertex displacement, which is equal to the nodal displacement of the truss model, denoted by the vector $\delta\mathbf{X} \in \mathbb{R}^{N_x}$ ($N_x = 3N_n$), is calculated from Eq. (32) and represented as a linear combination of $\mathbf{v}_1, \dots, \mathbf{v}_{N_x}$ introduced in Section 3 as

$$\delta\mathbf{X} = a_1^f \mathbf{v}_1 + \dots + a_{N_x}^f \mathbf{v}_{N_x}, \quad (33)$$

where $a_1^f, \dots, a_{N_x}^f \in \mathbb{R}$ are the coefficients to be investigated in this section. When $\mathbf{v}_1, \dots, \mathbf{v}_{N_x}$ form a system of orthonormal bases of the N_x -dimensional vector space, we can obtain a_i^f ($i = 1, \dots, N_x$) by simply calculating the inner product of $\delta\mathbf{X}$ and \mathbf{v}_i . However, in particular, $\mathbf{v}_1, \dots, \mathbf{v}_{N_x}$ are not always orthogonal to each other nor necessarily unit vectors, as shown by the examples in Section 6. Therefore, transformation of the coefficients corresponding to the basis transformation is necessary. Here, the vertex displacement vector $\delta\mathbf{X}$ is rewritten by using the orthonormal bases $\mathbf{v}_1^o, \dots, \mathbf{v}_{N_x}^o \in \mathbb{R}^{N_x}$ of the N_x -dimensional vector space as follows:

$$\delta\mathbf{X} = a_1^o \mathbf{v}_1^o + \dots + a_{N_x}^o \mathbf{v}_{N_x}^o, \tag{34}$$

where the first N_f bases $\mathbf{v}_1^o, \dots, \mathbf{v}_{N_f}^o$ correspond to the infinitesimal mechanism modes. Then, we can calculate the coefficients $a_1^o, \dots, a_{N_x}^o \in \mathbb{R}$, which are related to the orthonormal bases $\mathbf{v}_1^o, \dots, \mathbf{v}_{N_x}^o$ as

$$a_i^o = \mathbf{v}_i^{oT} \delta\mathbf{X} \quad (i = 1, \dots, N_x). \tag{35}$$

\mathbf{v}_i ($i = 1, \dots, N_x$) can also be written as a linear combination of $\mathbf{v}_1^o, \dots, \mathbf{v}_{N_x}^o$. Two matrices $\mathbf{V} = [\mathbf{v}_1 \dots \mathbf{v}_{N_x}] \in \mathbb{R}^{N_x \times N_x}$ and $\mathbf{V}^o = [\mathbf{v}_1^o \dots \mathbf{v}_{N_x}^o] \in \mathbb{R}^{N_x \times N_x}$ satisfy the following equation:

$$\mathbf{V} = \mathbf{V}^o \mathbf{T}, \tag{36}$$

where $\mathbf{T} \in \mathbb{R}^{N_x \times N_x}$ is a full-rank matrix whose i th column ($i = 1, \dots, N_x$) is the vector of coefficients for \mathbf{v}_i represented as a linear combination of $\mathbf{v}_1^o, \dots, \mathbf{v}_{N_x}^o$. According to Eqs. (33) and (34), when \mathbf{V} and \mathbf{V}^o satisfy Eq. (36), the coefficient vector $\mathbf{a}^f = (a_1^f \dots, a_{N_x}^f)^T \in \mathbb{R}^{N_x}$ can be obtained from $\mathbf{a}^o = (a_1^o \dots, a_{N_x}^o)^T \in \mathbb{R}^{N_x}$, which is determined by Eq. (35), as follows:

$$\mathbf{V}^o \mathbf{T} \mathbf{a}^f = \mathbf{V}^o \mathbf{a}^o \Leftrightarrow \mathbf{a}^f = \mathbf{T}^{-1} \mathbf{a}^o. \tag{37}$$

Here, we used the fact and assumption that $\mathbf{V}^{oT} \mathbf{V}^o$ and \mathbf{T} are an $N_x \times N_x$ identity matrix and a full-rank matrix, respectively. As mentioned in Remark 1, \mathbf{V}^o can be obtained as the right singular matrix of the compatibility matrix $d\mathbf{C}/d\mathbf{X}$.

Remark 3. The coefficients obtained by following the procedure introduced in this section are not exactly the same as the coefficients of the first-order infinitesimal mechanism \mathbf{a} in Eq. (16). The first N_f components of \mathbf{a}^f are the sums of the corresponding components of the coefficient vectors $\mathbf{a}^{(n)}$ in Eq. (23) for all $n \in \mathbb{N}$, and the remaining components are the sums of the corresponding components of $\mathbf{b}^{(n)}$. However, the first N_f components of \mathbf{a}^f obtained from Eq. (37) approximate those of $\mathbf{a}^{(1)}$ and approximately satisfy the quadratic Eqs. (17), as demonstrated in the examples in Section 6, especially when the deformation is small. Therefore, we classify the obtained path by comparing the coefficients obtained from the large deformation analysis and the solutions to Eq. (17).

6. Examples

In this section, the infinitesimal mechanism analysis given in Section 3 is applied to several basic crease patterns in which the quadratic Eqs. (17) can be analytically solved, and the coefficients of the mechanism modes are investigated by following the procedure described in Section 5. From the solutions to Eq. (17), we find that the bifurcation of the folding path occurs in the flat state and that some infinitesimal mechanism modes disappear in the finite motion if quadrilateral faces are included in a rigid origami.

In the large deformation analysis, the same material, member cross section, and hinge rotational stiffness are used for all the crease patterns. The pipe section is used in the frame members modeled by B31 beam elements in Abaqus, and the Young's modulus, Poisson's ratio, outer diameter, and wall thickness are 1.0×10^{11} kN/m², 0.3, 0.02 m, and 0.001 m, respectively. The rotational stiffness of the hinges is 0.01 kN·m. The nodal loads and displacement boundary conditions applied to the frame model are described in each example.

6.1. Miura-based pattern

In this subsection, the Miura-based pattern model shown in Fig. 4 is investigated. It has 8 vertices, 4 triangular faces, 2 quadrilateral faces, and 7 crease lines. The corresponding truss model has 8 nodes placed at the vertices and 17 bars placed along the edges and the diagonals of the faces. The node and bar indices and the initial nodal positions are shown in Fig. 4. The bar indices in Fig. 4 are also used as the indices of the crease lines. All the z -coordinates of nodes equal zero in the initial state.

6.1.1. First-order infinitesimal mechanism

The size of the compatibility matrix $d\mathbf{C}/d\mathbf{X}$ is 17×24 , and its rank is 13 in the flat state shown in Fig. 4. Therefore, the model has $24 - 13 - 6 = 5$ non-trivial infinitesimal mechanism modes and $17 - 13 = 4$ self-equilibrium force density modes. Note that the six infinitesimal mechanism modes corresponding to the rigid-body motion do not affect the results of the analysis in this and the following subsections. Figs. 5 and 6 show the nodal displacements in each non-trivial infinitesimal mechanism mode and the axial bar forces in each self-equilibrium force density mode, respectively. In the first-order infinitesimal mechanism, all the nodes move only in the z -direction. The components of the non-trivial infinitesimal mechanism modes $\mathbf{v}_1, \dots, \mathbf{v}_5$ and the self-equilibrium force density modes $\mathbf{u}_1, \dots, \mathbf{u}_4$ are summarized in Tables 1 and 2, respectively. They are empirically determined by considering

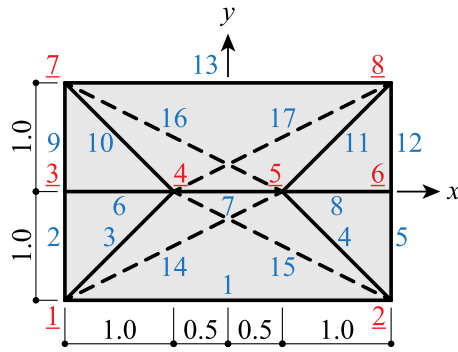


Fig. 4. Miura-based pattern in the initial flat state. Node indices are written in red with underlines, bar indices are written in blue, and the bars of the truss model placed along the diagonals are represented by dashed lines. (For interpretation of the references to color in this figure legend, the reader is referred to the web version of this article.)

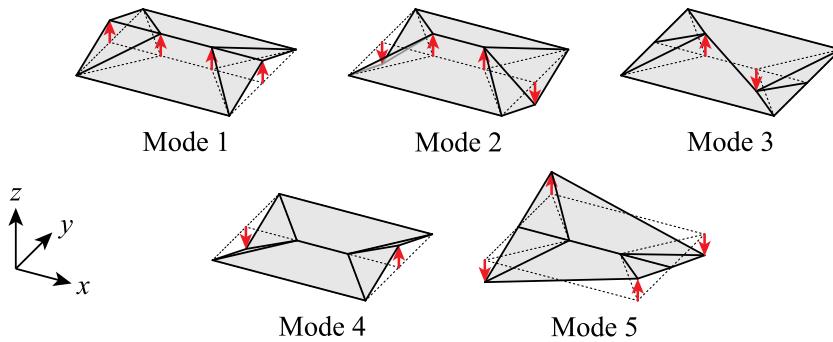


Fig. 5. Nodal displacements in non-trivial infinitesimal mechanism modes of Miura-based model. Vectors indicated by red arrows are unit vectors in the z -direction. In modes 3 and 5, two quadrilateral faces are bent in the out-of-plane direction. (For interpretation of the references to color in this figure legend, the reader is referred to the web version of this article.)

Table 1

Components of non-trivial infinitesimal mechanism modes v_1, \dots, v_5 of Miura-based model; all components corresponding to the x - and y -directions are zero.

Mode	z'_1	z'_2	z'_3	z'_4	z'_5	z'_6	z'_7	z'_8
1	0	0	1	1	1	1	0	0
2	0	0	-1	1	1	-1	0	0
3	0	0	0	1	-1	0	0	0
4	0	0	-1	0	0	1	0	0
5	-1	1	0	0	0	0	1	-1

the symmetry conditions. The first two infinitesimal mechanism modes and the first two self-equilibrium force density modes are symmetric with respect to both the xz - and yz -planes. Infinitesimal mechanism modes 3 and 4 and self-equilibrium force density mode 4 are antisymmetric with respect to the yz -plane while symmetric with respect to the xz -plane. Infinitesimal mechanism mode 5 is antisymmetric with respect to both the xz - and yz -planes, and self-equilibrium force density mode 3 is antisymmetric with respect to the xz -plane.

A non-trivial first-order infinitesimal mechanism can be expressed by using five coefficients $a_1, \dots, a_5 \in \mathbb{R}$ as Eq. (16). For a second-order infinitesimal mechanism to exist, these coefficients need to satisfy the following four quadratic equations obtained from Eq. (17) for the modes in Tables 1 and 2:

$$\begin{cases} 72a_3^2 + 8a_5^2 = 0 \\ -48a_1a_2 - 36a_3^2 + 12a_4^2 + 8a_5^2 = 0 \\ 48a_3a_5 = 0 \\ -24a_1a_3 - 8a_1a_4 - 24a_2a_3 + 8a_2a_4 = 0 \end{cases} \Leftrightarrow \begin{cases} 9a_3^2 + a_5^2 = 0 \\ 12a_1a_2 + 9a_3^2 - 3a_4^2 - 2a_5^2 = 0 \\ a_3a_5 = 0 \\ 3a_1a_3 + a_1a_4 + 3a_2a_3 - a_2a_4 = 0. \end{cases} \quad (38)$$

According to the first and third equations in Eq. (38), a_3 and a_5 need to satisfy

$$a_3 = a_5 = 0, \quad (39)$$

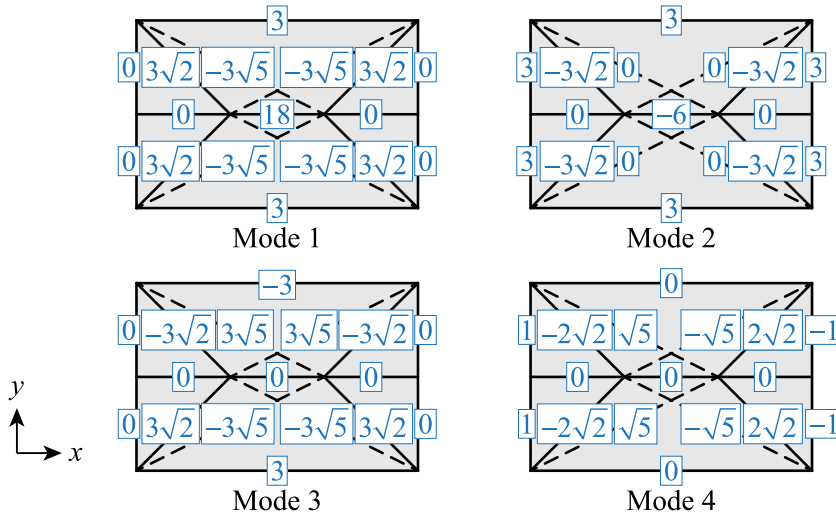


Fig. 6. Axial bar forces ω_{li} calculated from self-equilibrium force density modes of Miura-based model. Positive and negative values correspond to tension and compression forces, respectively. In modes 1 and 3, the axial forces exist only in the bars included in the quadrilateral faces.

Table 2
Components of self-equilibrium force density modes $\mathbf{u}_1, \dots, \mathbf{u}_4$ of the Miura-based model.

Mode	ω_1	ω_2	ω_3	ω_4	ω_5	ω_6	ω_7	ω_8	ω_9
1	1	0	3	3	0	0	18	0	0
2	1	3	-3	-3	3	0	-6	0	3
3	1	0	3	3	0	0	0	0	0
4	0	1	-2	2	-1	0	0	0	1
Mode	ω_{10}	ω_{11}	ω_{12}	ω_{13}	ω_{14}	ω_{15}	ω_{16}	ω_{17}	
1	3	3	0	1	-3	-3	-3	-3	
2	-3	-3	3	1	0	0	0	0	
3	-3	-3	0	-1	-3	-3	3	3	
4	-2	2	-1	0	1	-1	1	-1	

and the remaining equations are rewritten as

$$\begin{cases} 4a_1 a_2 - a_4^2 = 0 \\ (a_1 - a_2) a_4 = 0. \end{cases} \quad (40)$$

Therefore, the folding path corresponding to the non-trivial first-order infinitesimal mechanism that satisfies the condition for the existence of the second-order infinitesimal mechanism can be classified into the following four patterns using an arbitrary coefficient a_1 or a_2 as

$$\begin{aligned} \text{Path 1: } \mathbf{X}' &= a_1 \mathbf{v}_1 + a_1 \mathbf{v}_2 + 2a_1 \mathbf{v}_4, \\ \text{Path 2: } \mathbf{X}' &= a_1 \mathbf{v}_1 + a_1 \mathbf{v}_2 - 2a_1 \mathbf{v}_4, \\ \text{Path 3: } \mathbf{X}' &= a_1 \mathbf{v}_1, \\ \text{Path 4: } \mathbf{X}' &= a_2 \mathbf{v}_2. \end{aligned} \quad (41)$$

These four paths intersect only in the initial flat state $a_1 = a_2 = 0$ in the vicinity of the initial flat state, and we can conclude that this flat state is the bifurcation point of these four types of paths. It should be noted that the number of types of bifurcation paths may be reduced when the third- or higher-order infinitesimal mechanisms are considered in a general crease pattern, while this is not the case in the examples in this paper.

6.1.2. Observation of results of infinitesimal mechanism analysis

From Eq. (39), we can say that the finite mechanism does not exist in the direction of the infinitesimal mechanism mode where the quadrilateral faces are bent. This is in good agreement with the conclusion in Section 4.

The four bifurcation paths listed in Eq. (41) can be understood by distinguishing the crease lines into mountain and valley folds based on the directions of the folding angle increment. In each path, the symmetry of the model with respect to the xz -plane is preserved.

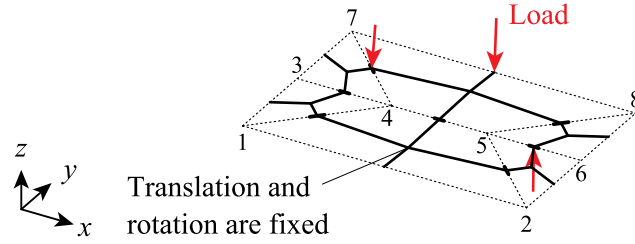


Fig. 7. Frame model of Miura-based model for large deformation analysis. Translation and rotation of the node on the face whose vertices are 1, 2, 4, and 5 are constrained, and nodal loads are applied to three randomly selected nodes as indicated by red arrows.

Path 1: Crease lines 3, 7, 8, and 10 are folded in the same direction; crease line 6 is folded in the opposite direction; and crease lines 4 and 11 are not folded.

Path 2: The mountain-valley assignment is mirrored with respect to the yz -plane from path 1.

Path 3: Diagonal crease lines 3, 4, 10, and 11 do not rotate, and crease lines 6, 7, and 8 rotate in the same direction.

Path 4: Crease lines 3, 4, 7, 10, and 11 rotate in the same direction, and crease lines 6 and 8 rotate in the opposite direction.

Each of the four paths listed in Eq. (41) is parametrized by a single parameter. In other words, the model in Fig. 4 has a single-degree-of-freedom mechanism once it deviates from the flat state $a_1 = a_2 = 0$. This is well-known feature of Miura-based crease patterns.

From Eq. (38), we can also observe the relationship between the infinitesimal modes and the self-equilibrium force density modes. The first and third equations in Eq. (38) are obtained from the self-equilibrium force density modes 1 and 3, where the axial forces exist only in the bars included in the quadrilateral faces, and in these two equations, only the coefficients corresponding to the infinitesimal mechanism modes 3 and 5, in which the quadrilateral faces are bent, are included. Both self-equilibrium force density modes 1 and 3 can be decomposed into the local self-equilibrium modes where a single quadrilateral face is in self-equilibrium and the other bars have zero axial force. Therefore, the first and third equations in Eq. (38) implies that the local self-equilibrium forces at each quadrilateral face only constrain the deformation of the face where the local self-equilibrium state is achieved.

6.1.3. Comparison to large deformation analysis

The frame model for the large deformation analysis of the Miura-based pattern is shown in Fig. 7. Translation and rotation of the node on the face whose vertices are 1, 2, 4, and 5 are constrained to avoid rigid-body motion of the entire model. The nodal loads are applied to three randomly selected nodes except for the nodes connected to the fixed node. The magnitude and direction of each nodal load are randomly determined so that its components in the x - and y -directions vary between -0.05 and 0.05 and the component in the z -direction varies between -0.5 and 0.5 . One hundred folding paths are obtained from the large deformation analysis, and the coefficients of the infinitesimal mechanism modes are calculated from the nodal displacements of the frame model by following the procedure introduced in Section 5. As stated in Remark 3, the coefficients investigated in this subsection, denoted by a_1^f, \dots, a_5^f , are not identical to but approximate the coefficients a_1, \dots, a_5 , which are the coefficients in the first-order infinitesimal mechanism, when the deformation of the rigid origami is small. However, for simplicity, the coefficients for each deformed state in the large deformation analysis are denoted by a_1, \dots, a_5 instead of a_1^f, \dots, a_5^f in the following analysis. The obtained large deformation paths are classified into the four types shown in Eq. (41) based on the values of the coefficients in each deformed state in the large deformation analysis. Because the coefficients may not exactly satisfy Eq. (38), each deformed state is classified based on the following criteria, in which the existence of the errors in the coefficients is assumed:

Path 1: $a_1 a_4 \geq 0$ and $|a_4| \geq \max(|a_1|, |a_2|)/1000$,

Path 2: $a_1 a_4 < 0$ and $|a_4| \geq \max(|a_1|, |a_2|)/1000$,

Path 3: $|a_1| > |a_2|$ and $|a_4| < |a_1|/1000$,

Path 4: $|a_1| < |a_2|$ and $|a_4| < |a_2|/1000$.

Especially when the deformation is quite small, the deformed states at the consecutive analysis steps may be classified into different types of bifurcation paths. Therefore, the entire path is classified into the type of bifurcation path that appears most frequently in the deformed states on the path.

Figs. 8, 9, and 10 show the transition of the maximum absolute value of the strain among the edges at each analysis step, the value of the left-hand sides of the quadratic Eqs. (38), and the coefficients a_1, \dots, a_5 for several coefficient pairs, respectively. The folding processes on the obtained paths indicated by the bold lines in Figs. 8 and 10 are shown in Fig. 11. The four line types in Figs. 8 and 10 represent the classification of the obtained path according to the above criteria. The folding properties investigated in Section 6.1.2 with respect to the first-order infinitesimal mechanism can also be confirmed by the large deformation analysis, as shown in Fig. 11; the quadrilateral faces are not bent, and the mountain-valley assignments are consistent with the observation in Section 6.1.2.

It can be seen from Fig. 8 that the absolute value of the strain for each edge is less than 0.6×10^{-4} throughout the large deformation analysis, and the obtained paths can be approximately regarded as rigid-folding paths. The quadratic Eqs. (38) are also well satisfied,

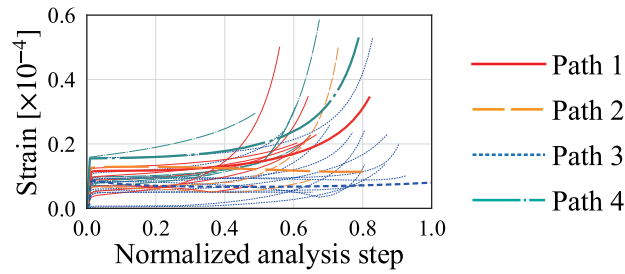


Fig. 8. Maximum absolute strain among edges (absolute values of edge length changes divided by initial lengths) along some folding paths of Miura-based model selected so that the path with the largest maximum strain are included for each bifurcation path. The value corresponding to the horizontal axis at each analysis step represents the maximum trajectory length among the vertices, which is normalized so that the maximum value among all the paths and steps is equal to 1.0. Strain values are small, and all the paths can be approximately regarded as rigid-folding paths.

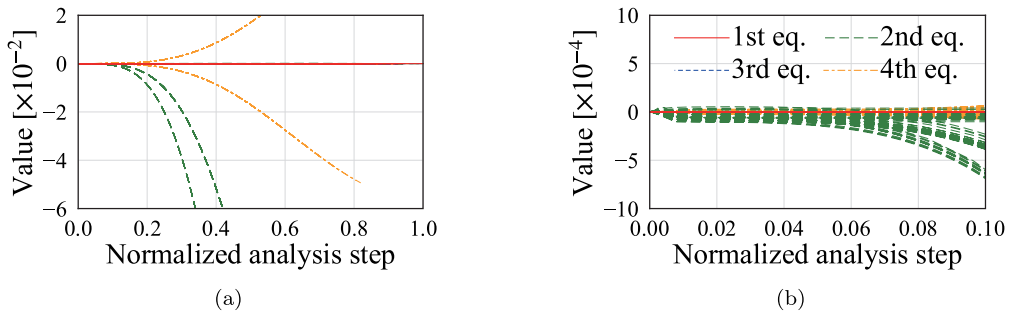


Fig. 9. Values of left-hand sides of quadratic Eqs. (38) over a_1, \dots, a_5 , which are fairly small in the vicinity of the initial flat state: (a) overall view and (b) detailed view.

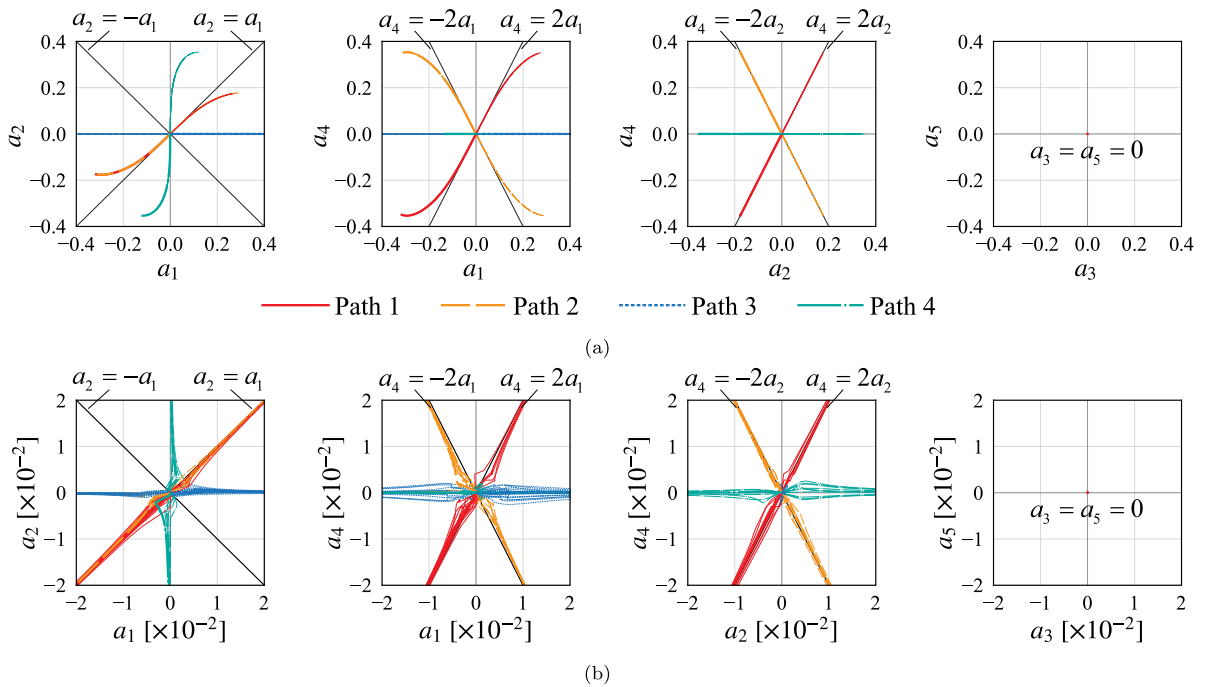


Fig. 10. Values of coefficients of infinitesimal mechanism modes a_1, \dots, a_5 on the folding paths of Miura-based model: (a) overall view and (b) detailed view. In the first, second, and third columns, the coefficients satisfying Eq. (38) need to be on the black diagonal lines.

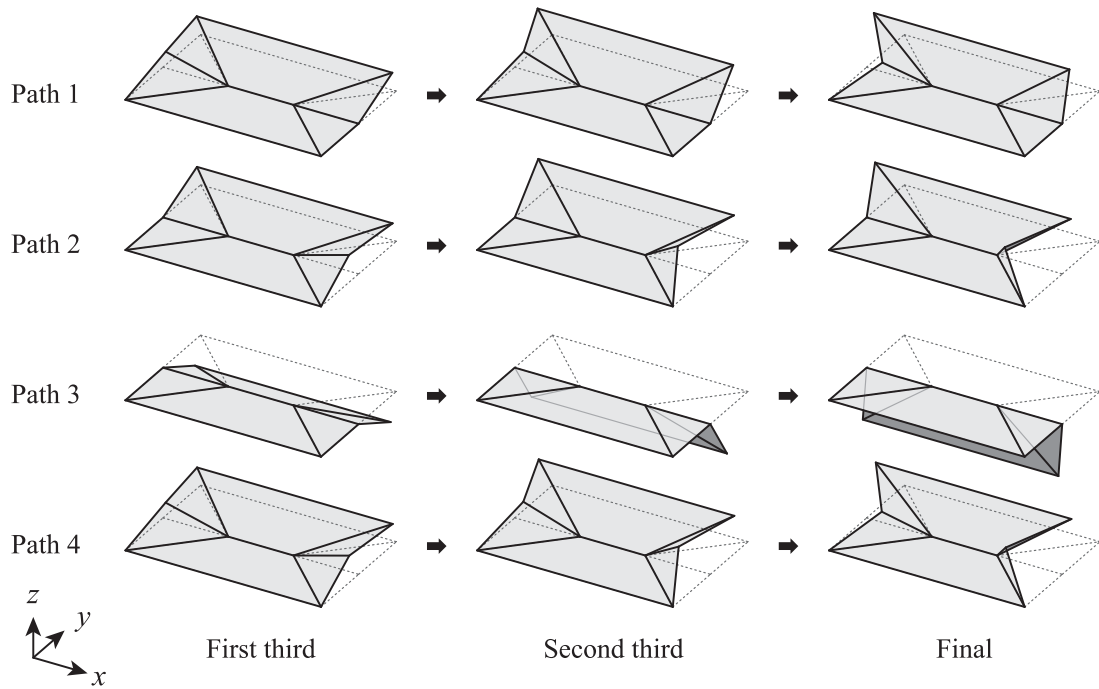


Fig. 11. Folding sequences obtained in large deformation analysis of Miura-based model corresponding to bold lines in Fig. 10. The first, second, and third columns are deformed shapes at the first third, second third, and end of folding path, respectively.

as can be seen in Fig. 9 in the vicinity of the initial flat state. However, the values of the left-hand sides of the second and fourth equations increase as the analysis progresses. These increases can be attributed to the fact that the coefficients a_1, \dots, a_5 are not strictly the coefficients in the first-order infinitesimal mechanism as stated in Remark 3. Fig. 10 shows that a_3 and a_5 , which need to be zero from Eq. (38), are approximately equal to zero throughout the large deformation analysis. Furthermore, the values of a_1, a_2 , and a_4 , which need to be on the black inclined lines in Fig. 10, satisfy the relationship obtained from Eq. (40) only near the origin, and they drift away from the black lines as the analysis progresses, in correspondence with the increasing values of the left-hand sides in the quadratic equations. From the above observations, we can conclude that the coefficients of the infinitesimal mechanism modes obtained from the large deformation analysis closely approximate the coefficients in the first-order infinitesimal mechanism in the small deformation range. When the deformation is large, the coefficients investigated here may include the terms for the higher-order infinitesimal mechanisms, as stated in Remark 2. As shown in Fig. 10(b), jumps between the bifurcation paths are observed near the flat state. However, as the large deformation analysis progresses, each trajectory of the coefficients tends to converge to a single curve corresponding to one of four bifurcation paths. This reflects the fact that the degrees of freedom of the mechanism become one when the model deviates from the flat state.

6.2. Double-waterbomb cells

In this subsection, the double-waterbomb cells pattern model (DWC model) shown in Fig. 12 is investigated. It has 11 vertices, 12 triangular faces, and 14 crease lines. The corresponding truss model has 11 nodes at the vertices and 22 bars along the edges. The indices of nodes and bars and the initial nodal positions are shown in Fig. 12. All the z -coordinates of nodes are equal to zero in the initial state.

6.2.1. First-order infinitesimal mechanism

The size of the compatibility matrix dC/dX is 22×33 , and its rank is 19 in the flat state shown in Fig. 12. Therefore, the DWC model has $33 - 19 - 6 = 8$ non-trivial infinitesimal mechanism modes and $22 - 19 = 3$ self-equilibrium force density modes. Figs. 13 and 14 show the nodal displacements in each non-trivial infinitesimal mechanism mode and the axial bar forces in each self-equilibrium force density mode, respectively. In the first-order infinitesimal mechanism, all the nodes move only in the z -direction. The components of the non-trivial infinitesimal mechanism modes v_1, \dots, v_8 and the self-equilibrium force density modes u_1, u_2, u_3 are summarized in Tables 3 and 4, respectively. The first four infinitesimal mechanism modes and the first two self-equilibrium force density modes are symmetric with respect to both the xz - and yz -planes. Infinitesimal mechanism modes 5 and 6 and self-equilibrium force density mode 3 are antisymmetric with respect to the yz -plane but symmetric with respect to the xz -plane. Infinitesimal mechanism mode 7 is antisymmetric with respect to both the xz - and yz -planes, and infinitesimal mechanism mode 8 is antisymmetric with respect to the xz -plane.

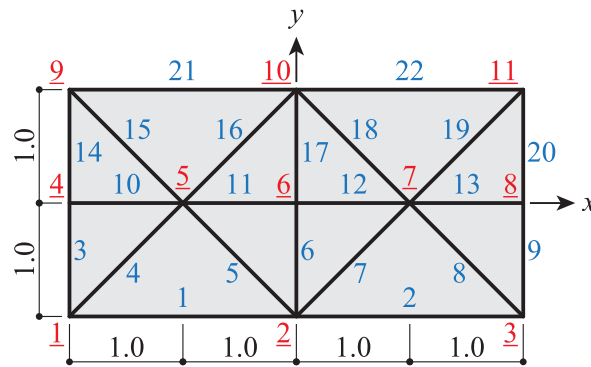


Fig. 12. Double-waterbomb cells pattern in the initial flat state. Node indices are written in red with underlines and bar indices are written in blue. (For interpretation of the references to color in this figure legend, the reader is referred to the web version of this article.)

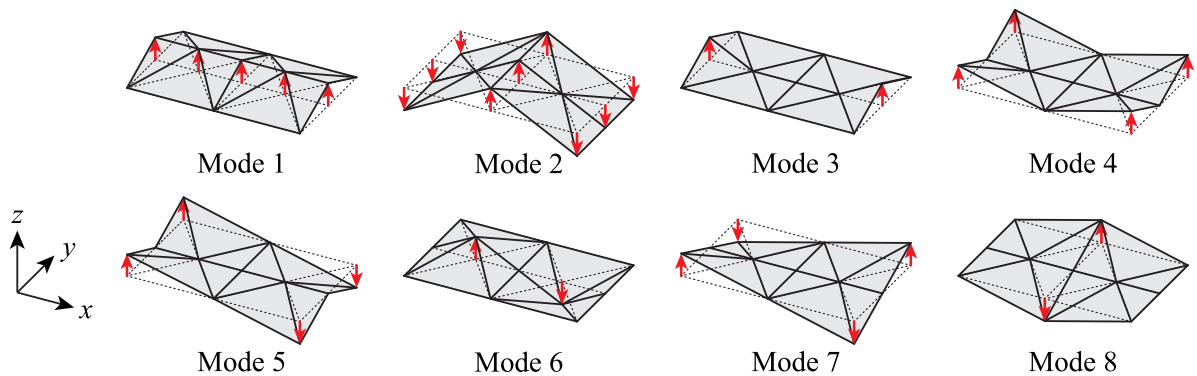


Fig. 13. Nodal displacements in the non-trivial infinitesimal mechanism modes of the DWC model; vectors indicated by red arrows are unit vectors in the z-direction. Four crease lines at the center are folded only in modes 1 and 2.

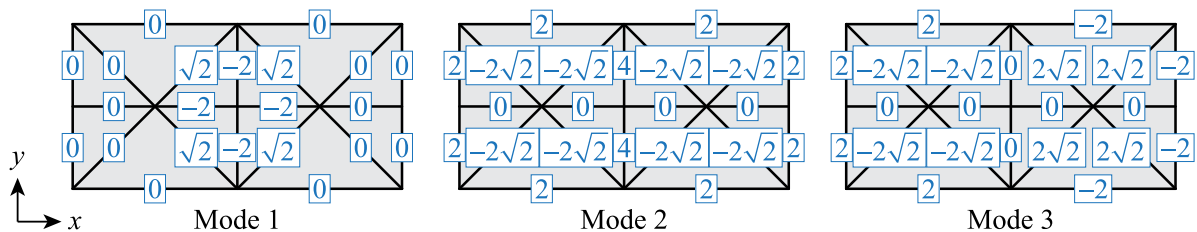


Fig. 14. Axial bar forces ω_i/l_i calculated from the self-equilibrium force density modes of the DWC model. Positive and negative values correspond to tension and compression forces, respectively.

Table 3

Components of non-trivial infinitesimal mechanism modes $\mathbf{v}_1, \dots, \mathbf{v}_8$ of DWC model; all components corresponding to the x- and y-directions are zero.

Mode	z'_1	z'_2	z'_3	z'_4	z'_5	z'_6	z'_7	z'_8	z'_9	z'_{10}	z'_{11}
1	0	0	0	1	1	1	1	1	0	0	0
2	-1	1	-1	-1	0	1	0	-1	-1	1	-1
3	0	0	0	1	0	0	0	1	0	0	0
4	1	0	1	0	0	0	0	0	1	0	1
5	1	0	-1	0	0	0	0	0	1	0	-1
6	0	0	0	0	1	0	-1	0	0	0	0
7	1	0	-1	0	0	0	0	0	-1	0	1
8	0	-1	0	0	0	0	0	0	0	1	0

Table 4
Components of self-equilibrium force density modes $\mathbf{u}_1, \mathbf{u}_2, \mathbf{u}_3$ of the DWC model.

Mode	ω_1	ω_2	ω_3	ω_4	ω_5	ω_6	ω_7	ω_8	ω_9	ω_{10}	ω_{11}
1	0	0	0	0	1	-2	1	0	0	0	-2
2	1	1	2	-2	-2	4	-2	-2	2	0	0
3	1	-1	2	-2	-2	0	2	2	-2	0	0
Mode	ω_{12}	ω_{13}	ω_{14}	ω_{15}	ω_{16}	ω_{17}	ω_{18}	ω_{19}	ω_{20}	ω_{21}	ω_{22}
1	-2	0	0	0	1	-2	1	0	0	0	0
2	0	0	2	-2	-2	4	-2	-2	2	1	1
3	0	0	2	-2	-2	0	2	2	-2	1	-1

A non-trivial first-order infinitesimal mechanism can be expressed by using eight coefficients $a_1, \dots, a_8 \in \mathbb{R}$ as Eq. (16). The existence condition of a second-order infinitesimal mechanism is represented by the following three quadratic equations for the modes in Tables 3 and 4:

$$\begin{cases} -8a_1a_2 = 0 \\ 16a_1a_3 + 8a_3^2 - 16a_3a_4 + 4a_4^2 + 4a_5^2 + 16a_5a_6 - 16a_6^2 + 4a_7^2 + 4a_8^2 = 0 \\ -32a_1a_6 - 16a_3a_5 + 8a_4a_5 + 16a_4a_6 + 8a_7a_8 = 0 \end{cases} \tag{42}$$

$$\Leftrightarrow \begin{cases} a_1a_2 = 0 \\ 4a_1a_3 + 2a_3^2 - 4a_3a_4 + a_4^2 + a_5^2 + 4a_5a_6 - 4a_6^2 + a_7^2 + a_8^2 = 0 \\ 4a_1a_6 + 2a_3a_5 - a_4a_5 - 2a_4a_6 - a_7a_8 = 0. \end{cases}$$

By adding the third equation multiplied by 2 and -2 to the second equation, respectively, Eq. (42) is equivalently transformed as follows:

$$\begin{cases} a_1a_2 = 0 \\ 2a_1^2 - 2(a_1 - a_3 - 2a_6)^2 + (2a_3 - a_4 + a_5 + 2a_6)^2 + (a_7 - a_8)^2 = 0 \\ 2a_1^2 - 2(a_1 - a_3 + 2a_6)^2 + (2a_3 - a_4 - a_5 - 2a_6)^2 + (a_7 + a_8)^2 = 0. \end{cases} \tag{43}$$

Here, we replace the coefficients a_1, \dots, a_8 with $\bar{a}_1, \dots, \bar{a}_8$ so that

$$\begin{cases} a_1 = \bar{a}_1 \\ a_2 = \bar{a}_2 \\ a_3 = \bar{a}_1 - 2\bar{a}_3 - 2\bar{a}_4 \\ a_4 = 2\bar{a}_1 - 4\bar{a}_3 - 4\bar{a}_4 - \bar{a}_5 - \bar{a}_6 \\ a_5 = 2\bar{a}_3 - 2\bar{a}_4 + \bar{a}_5 - \bar{a}_6 \\ a_6 = -\bar{a}_3 + \bar{a}_4 \\ a_7 = \bar{a}_7 + \bar{a}_8 \\ a_8 = -\bar{a}_7 + \bar{a}_8 \end{cases} \Leftrightarrow \begin{cases} \bar{a}_1 = a_1 \\ \bar{a}_2 = a_2 \\ \bar{a}_3 = \frac{1}{4}(a_1 - a_3 - 2a_6) \\ \bar{a}_4 = \frac{1}{4}(a_1 - a_3 + 2a_6) \\ \bar{a}_5 = \frac{1}{2}(2a_3 - a_4 + a_5 + 2a_6) \\ \bar{a}_6 = \frac{1}{2}(2a_3 - a_4 - a_5 - 2a_6) \\ \bar{a}_7 = \frac{1}{2}(a_7 - a_8) \\ \bar{a}_8 = \frac{1}{2}(a_7 + a_8), \end{cases} \tag{44}$$

and reformulate Eq. (43) as follows:

$$\begin{cases} \bar{a}_1\bar{a}_2 = 0 \\ \bar{a}_1^2 - 16\bar{a}_3^2 + 2\bar{a}_5^2 + 2\bar{a}_7^2 = 0 \\ \bar{a}_1^2 - 16\bar{a}_4^2 + 2\bar{a}_6^2 + 2\bar{a}_8^2 = 0. \end{cases} \tag{45}$$

The infinitesimal mechanism modes $\mathbf{v}_1, \dots, \mathbf{v}_8$ corresponding to a_1, \dots, a_8 are replaced with $\bar{\mathbf{v}}_1, \dots, \bar{\mathbf{v}}_8$ corresponding to $\bar{a}_1, \dots, \bar{a}_8$ based on the following equation:

$$\begin{aligned} a_1\mathbf{v}_1 + a_2\mathbf{v}_2 + \dots + a_8\mathbf{v}_8 &= \bar{a}_1(\mathbf{v}_1 + \mathbf{v}_3 + 2\mathbf{v}_4) + \bar{a}_2\mathbf{v}_2 \\ &\quad + \bar{a}_3(-2\mathbf{v}_3 - 4\mathbf{v}_4 + 2\mathbf{v}_5 - \mathbf{v}_6) \\ &\quad + \bar{a}_4(-2\mathbf{v}_3 - 4\mathbf{v}_4 - 2\mathbf{v}_5 + \mathbf{v}_6) \\ &\quad + \bar{a}_5(-\mathbf{v}_4 + \mathbf{v}_5) + \bar{a}_6(-\mathbf{v}_4 - \mathbf{v}_5) \\ &\quad + \bar{a}_7(\mathbf{v}_7 - \mathbf{v}_8) + \bar{a}_8(\mathbf{v}_7 + \mathbf{v}_8) \\ &= \bar{a}_1\bar{\mathbf{v}}_1 + \bar{a}_2\bar{\mathbf{v}}_2 + \dots + \bar{a}_8\bar{\mathbf{v}}_8. \end{aligned} \tag{46}$$

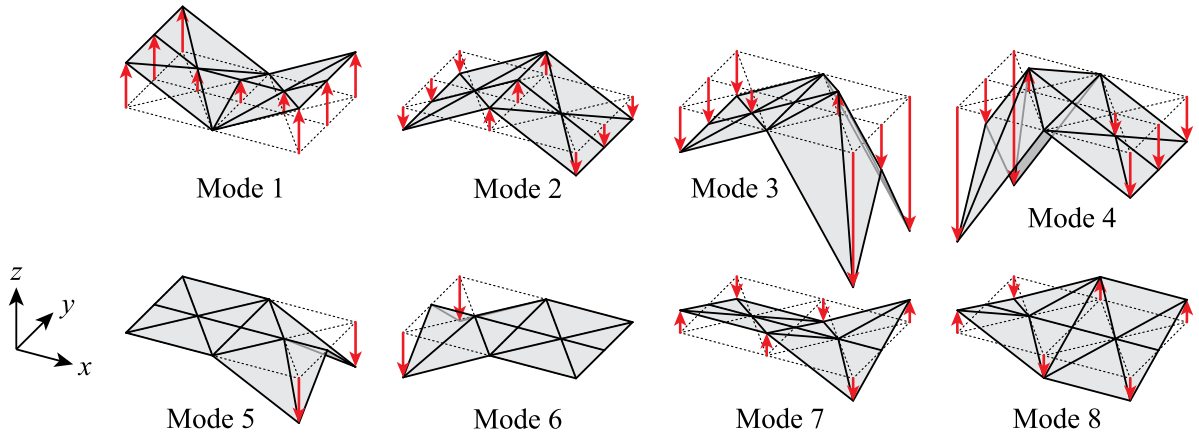


Fig. 15. Nodal displacements in modified non-trivial infinitesimal mechanism modes of DWC model obtained from Eq. (46). Red arrows represent the nodal displacements in the z -direction whose lengths indicate the ratio of the displacement. Four crease lines at the center are folded only in modes 1 and 2.

Table 5
Components of modified non-trivial infinitesimal mechanism modes $\bar{v}_1, \dots, \bar{v}_8$ of DWC model obtained from Eq. (46).

Mode	z'_1	z'_2	z'_3	z'_4	z'_5	z'_6	z'_7	z'_8	z'_9	z'_{10}	z'_{11}
1	2	0	2	2	1	1	1	2	2	0	2
2	-1	1	-1	-1	0	1	0	-1	-1	1	-1
3	-2	0	-6	-2	-1	0	1	-2	-2	0	-6
4	-6	0	-2	-2	1	0	-1	-2	-6	0	-2
5	0	0	-2	0	0	0	0	0	0	0	-2
6	-2	0	0	0	0	0	0	0	-2	0	0
7	1	1	-1	0	0	0	0	0	-1	-1	1
8	1	-1	-1	0	0	0	0	0	-1	1	1

The infinitesimal mechanism modes $\bar{v}_1, \dots, \bar{v}_8$ obtained from Eq. (46) are shown in Fig. 15 and Table 5. We can always solve the second and third equations in Eq. (45) for \bar{a}_3 and \bar{a}_4 as follows:

$$\bar{a}_3 = \pm \frac{1}{4} \sqrt{\bar{a}_1^2 + 2\bar{a}_5^2 + 2\bar{a}_7^2}, \quad \bar{a}_4 = \pm \frac{1}{4} \sqrt{\bar{a}_1^2 + 2\bar{a}_6^2 + 2\bar{a}_8^2}. \tag{47}$$

Therefore, the non-trivial first-order infinitesimal mechanism that satisfies the condition for the existence of a second-order infinitesimal mechanism can be classified into eight patterns using arbitrary coefficients $\bar{a}_1, \bar{a}_2, \bar{a}_5, \dots, \bar{a}_8$ as

$$\begin{aligned} \text{Path 1: } \mathbf{X}' &= \bar{a}_1 \bar{v}_1 + A_{31} \bar{v}_3 + A_{41} \bar{v}_4 + \bar{a}_5 \bar{v}_5 + \bar{a}_6 \bar{v}_6 + \bar{a}_7 \bar{v}_7 + \bar{a}_8 \bar{v}_8, \\ \text{Path 2: } \mathbf{X}' &= \bar{a}_1 \bar{v}_1 - A_{31} \bar{v}_3 - A_{41} \bar{v}_4 + \bar{a}_5 \bar{v}_5 + \bar{a}_6 \bar{v}_6 + \bar{a}_7 \bar{v}_7 + \bar{a}_8 \bar{v}_8, \\ \text{Path 3: } \mathbf{X}' &= \bar{a}_1 \bar{v}_1 + A_{31} \bar{v}_3 - A_{41} \bar{v}_4 + \bar{a}_5 \bar{v}_5 + \bar{a}_6 \bar{v}_6 + \bar{a}_7 \bar{v}_7 + \bar{a}_8 \bar{v}_8, \\ \text{Path 4: } \mathbf{X}' &= \bar{a}_1 \bar{v}_1 - A_{31} \bar{v}_3 + A_{41} \bar{v}_4 + \bar{a}_5 \bar{v}_5 + \bar{a}_6 \bar{v}_6 + \bar{a}_7 \bar{v}_7 + \bar{a}_8 \bar{v}_8, \\ \text{Path 5: } \mathbf{X}' &= \bar{a}_2 \bar{v}_2 + A_{32} \bar{v}_3 + A_{42} \bar{v}_4 + \bar{a}_5 \bar{v}_5 + \bar{a}_6 \bar{v}_6 + \bar{a}_7 \bar{v}_7 + \bar{a}_8 \bar{v}_8, \\ \text{Path 6: } \mathbf{X}' &= \bar{a}_2 \bar{v}_2 - A_{32} \bar{v}_3 - A_{42} \bar{v}_4 + \bar{a}_5 \bar{v}_5 + \bar{a}_6 \bar{v}_6 + \bar{a}_7 \bar{v}_7 + \bar{a}_8 \bar{v}_8, \\ \text{Path 7: } \mathbf{X}' &= \bar{a}_2 \bar{v}_2 + A_{32} \bar{v}_3 - A_{42} \bar{v}_4 + \bar{a}_5 \bar{v}_5 + \bar{a}_6 \bar{v}_6 + \bar{a}_7 \bar{v}_7 + \bar{a}_8 \bar{v}_8, \\ \text{Path 8: } \mathbf{X}' &= \bar{a}_2 \bar{v}_2 - A_{32} \bar{v}_3 + A_{42} \bar{v}_4 + \bar{a}_5 \bar{v}_5 + \bar{a}_6 \bar{v}_6 + \bar{a}_7 \bar{v}_7 + \bar{a}_8 \bar{v}_8, \end{aligned} \tag{48}$$

where

$$\begin{aligned} A_{31} &= \frac{1}{4} \sqrt{\bar{a}_1^2 + 2\bar{a}_5^2 + 2\bar{a}_7^2}, & A_{41} &= \frac{1}{4} \sqrt{\bar{a}_1^2 + 2\bar{a}_6^2 + 2\bar{a}_8^2}, \\ A_{32} &= \frac{1}{4} \sqrt{2\bar{a}_5^2 + 2\bar{a}_7^2}, & A_{42} &= \frac{1}{4} \sqrt{2\bar{a}_6^2 + 2\bar{a}_8^2}. \end{aligned}$$

6.2.2. Observation of results of infinitesimal mechanism analysis

From the first equation in Eq. (45), we can see that among the four cross-shaped crease lines in the center, only one pair of two crease lines in the x -direction or one pair in the y -direction rotates, and the four crease lines do not rotate simultaneously. The first equation in Eq. (45) is obtained from the self-equilibrium force density mode 1, where the axial forces exist only in the center, and the coefficients included in the first equation are the infinitesimal mechanism modes 1 and 2, which are the only modes where the center is folded and the other parts are not folded, as shown in Fig. 15. This implies that, as observed in the Miura-based pattern

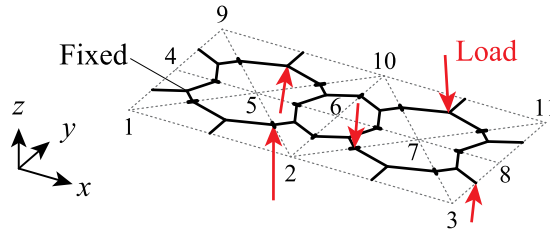


Fig. 16. Frame model of DWC model for large deformation analysis. Translation and rotation of the node on the face whose vertices are 1, 4, and 5 are constrained, and nodal loads are applied to five randomly selected nodes as indicated by red arrows.

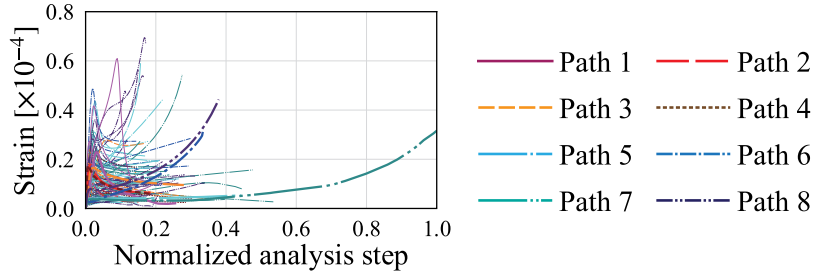


Fig. 17. Maximum absolute strain among edges along folding paths of DWC model. Strain values are small, and all the paths can be approximately regarded as rigid-folding paths.

model, the local self-equilibrium state constrains the local mechanism mode. This local behavior can also be observed in the second and third equations in Eq. (45). The self-equilibrium mode corresponding to the second equation can be obtained by subtracting the self-equilibrium force density mode 3 from mode 2 in Fig. 14, and in this mode, the axial forces exist only in the bars in the right half. The infinitesimal mechanism modes 3, 5, and 7 in Fig. 15, whose coefficients \bar{a}_3 , \bar{a}_5 , and \bar{a}_7 are included in the second equation, also have the local property that only the right part of the model is folded. Therefore, in the second equation, both the self-equilibrium force and the folded crease lines exist only in the right half of the model in Fig. 12. The same can be said for the third equation with the left and right sides exchanged.

6.2.3. Comparison to large deformation analysis

The frame model for the large deformation analysis of the DWC model is shown in Fig. 16. The translation and rotation of the node on the face whose vertices are 1, 4, and 5 are constrained to avoid rigid-body motion of the entire model. The nodal loads are applied to five randomly selected nodes except for the nodes connected to the fixed node, and their magnitude and direction are randomly determined in the same manner as in Section 6.1.3. One hundred folding paths are obtained from the large deformation analysis, and the deformed states on the obtained paths are classified based on the following criteria for the coefficients $\bar{a}_1 \dots, \bar{a}_8$:

- Path 1: $|\bar{a}_1| \geq |\bar{a}_2|$, $\bar{a}_3 \geq 0$, and $\bar{a}_4 \geq 0$,
- Path 2: $|\bar{a}_1| \geq |\bar{a}_2|$, $\bar{a}_3 < 0$, and $\bar{a}_4 < 0$,
- Path 3: $|\bar{a}_1| \geq |\bar{a}_2|$, $\bar{a}_3 \geq 0$, and $\bar{a}_4 < 0$,
- Path 4: $|\bar{a}_1| \geq |\bar{a}_2|$, $\bar{a}_3 < 0$, and $\bar{a}_4 \geq 0$,
- Path 5: $|\bar{a}_1| < |\bar{a}_2|$, $\bar{a}_3 \geq 0$, and $\bar{a}_4 \geq 0$,
- Path 6: $|\bar{a}_1| < |\bar{a}_2|$, $\bar{a}_3 < 0$, and $\bar{a}_4 < 0$,
- Path 7: $|\bar{a}_1| < |\bar{a}_2|$, $\bar{a}_3 \geq 0$, and $\bar{a}_4 < 0$,
- Path 8: $|\bar{a}_1| < |\bar{a}_2|$, $\bar{a}_3 < 0$, and $\bar{a}_4 \geq 0$.

Figs. 17, 18, and 19 show the transition of the maximum absolute value of the strain of the bars in the truss model, the value of the left-hand sides of the quadratic Eqs. (42), and the coefficients $\bar{a}_1 \dots, \bar{a}_8$ for several coefficient pairs, respectively. The folding processes on the obtained paths indicated by the bold lines in Figs. 17 and 19 are shown in Fig. 20. The eight line types in Figs. 17 and 19 represent the classification of the obtained paths.

The overall trend in the DWC model is basically the same as that for the Miura-based pattern investigated in Section 6.1.3. As shown in Figs. 17 and 18, the obtained paths are approximately rigid-folding paths, and the quadratic Eqs. (42) are well satisfied when the deformation is small. The gray hatched regions in Fig. 19 represent the regions where the values of the coefficients can exist. Most paths are within the indicated gray regions, whereas some of them cross the boundary to the regions where the coefficients cannot exist in the early stage of the analysis. This may be due to the jumps between the bifurcation paths caused by the numerical errors or the nature of the convergence calculations in the large deformation analysis. It can also be seen in Fig. 19 that the deformation paths mainly converge near the boundaries of the gray regions.

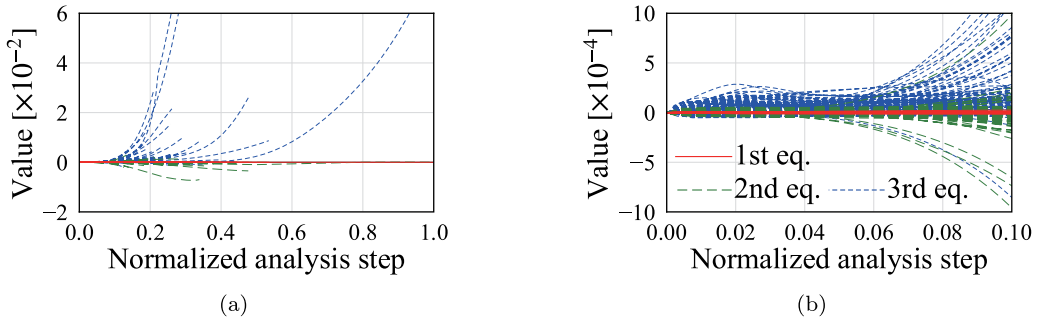


Fig. 18. Values of left-hand sides of Eq. (45) over $\bar{a}_1, \dots, \bar{a}_8$, which are fairly small in the vicinity of the initial flat state: (a) overall view and (b) detailed view.

Table 6

Components of non-trivial infinitesimal mechanism modes $\mathbf{v}_1, \dots, \mathbf{v}_9$ of flasher model; all components corresponding to the x - and y -directions are zero.

Mode	z'_1	z'_2	z'_3	z'_4	z'_5	z'_6	z'_7	z'_8	z'_9	z'_{10}	z'_{11}	z'_{12}
1	1	0	0	0	0	0	0	0	0	0	0	0
2	0	1	0	0	0	0	0	0	0	0	0	0
3	0	0	0	0	0	1	0	0	0	0	0	0
4	0	0	0	0	0	0	0	0	0	1	0	0
5	0	0	0	0	0	0	0	0	0	0	0	1
6	0	0	0	0	0	0	0	0	0	0	1	0
7	0	0	0	0	0	0	1	0	0	0	0	0
8	0	0	1	0	0	0	0	0	0	0	0	0
9	0	0	0	1	0	0	0	0	1	0	0	0

Table 7

Components of the self-equilibrium force density modes $\mathbf{u}_1, \dots, \mathbf{u}_5$ of the flasher model.

Mode	ω_1	ω_2	ω_3	ω_4	ω_5	ω_6	ω_7	ω_8	ω_9	ω_{10}	ω_{11}	ω_{12}	ω_{13}
1	0	0	0	0	0	0	0	1	0	0	0	1	-1
2	1	1	-1	-1	1	0	-2	0	0	0	1	-1	-1
3	0	0	0	1	-2	1	1	-1	-1	1	-1	0	1
4	1	1	-1	-1	1	0	-2	-1	0	0	1	-2	0
5	0	0	0	1	-2	1	-1	-2	-1	-1	1	1	0
Mode	ω_{14}	ω_{15}	ω_{16}	ω_{17}	ω_{18}	ω_{19}	ω_{20}	ω_{21}	ω_{22}	ω_{23}	ω_{24}	ω_{25}	ω_{26}
1	-1	1	0	0	0	1	0	0	0	0	0	0	0
2	1	-1	1	0	0	0	-2	0	1	-1	-1	1	1
3	-1	0	-1	1	-1	-1	1	1	-2	1	0	0	0
4	0	2	-1	0	0	1	2	0	-1	1	1	-1	-1
5	0	-1	-1	1	1	2	1	-1	2	-1	0	0	0

6.3. Flasher pattern

In this subsection, the flasher pattern model shown in Fig. 21 is investigated. It has 12 vertices, 12 triangular faces, 1 quadrilateral face, and 16 crease lines. The corresponding truss model has 12 nodes and 26 bars placed at the vertices and along the edges and diagonals, respectively. The indices of nodes and bars and the initial nodal positions are shown in Fig. 21. All the z -coordinates of nodes in the initial state are equal to zero.

6.3.1. First-order infinitesimal mechanism

The size of the compatibility matrix dC/dX is 26×36 , and its rank is 21 in the flat state shown in Fig. 21. Therefore, the flasher model has $36 - 21 - 6 = 9$ non-trivial infinitesimal mechanism modes and $26 - 21 = 5$ self-equilibrium force density modes. Figs. 22 and 23 show the nodal displacements in each non-trivial infinitesimal mechanism mode and the axial bar forces in each self-equilibrium force density mode, respectively. In the first-order infinitesimal mechanism, all the nodes move only in the z -direction. The components of the non-trivial infinitesimal mechanism modes $\mathbf{v}_1, \dots, \mathbf{v}_9$ and the self-equilibrium force density modes $\mathbf{u}_1, \dots, \mathbf{u}_5$ are summarized in Tables 6 and 7, respectively.

A non-trivial first-order infinitesimal mechanism can be expressed by using nine coefficients $a_1, \dots, a_9 \in \mathbb{R}$ as Eq. (16). For a second-order infinitesimal mechanism to exist, these coefficients need to satisfy the following five quadratic equations formulated

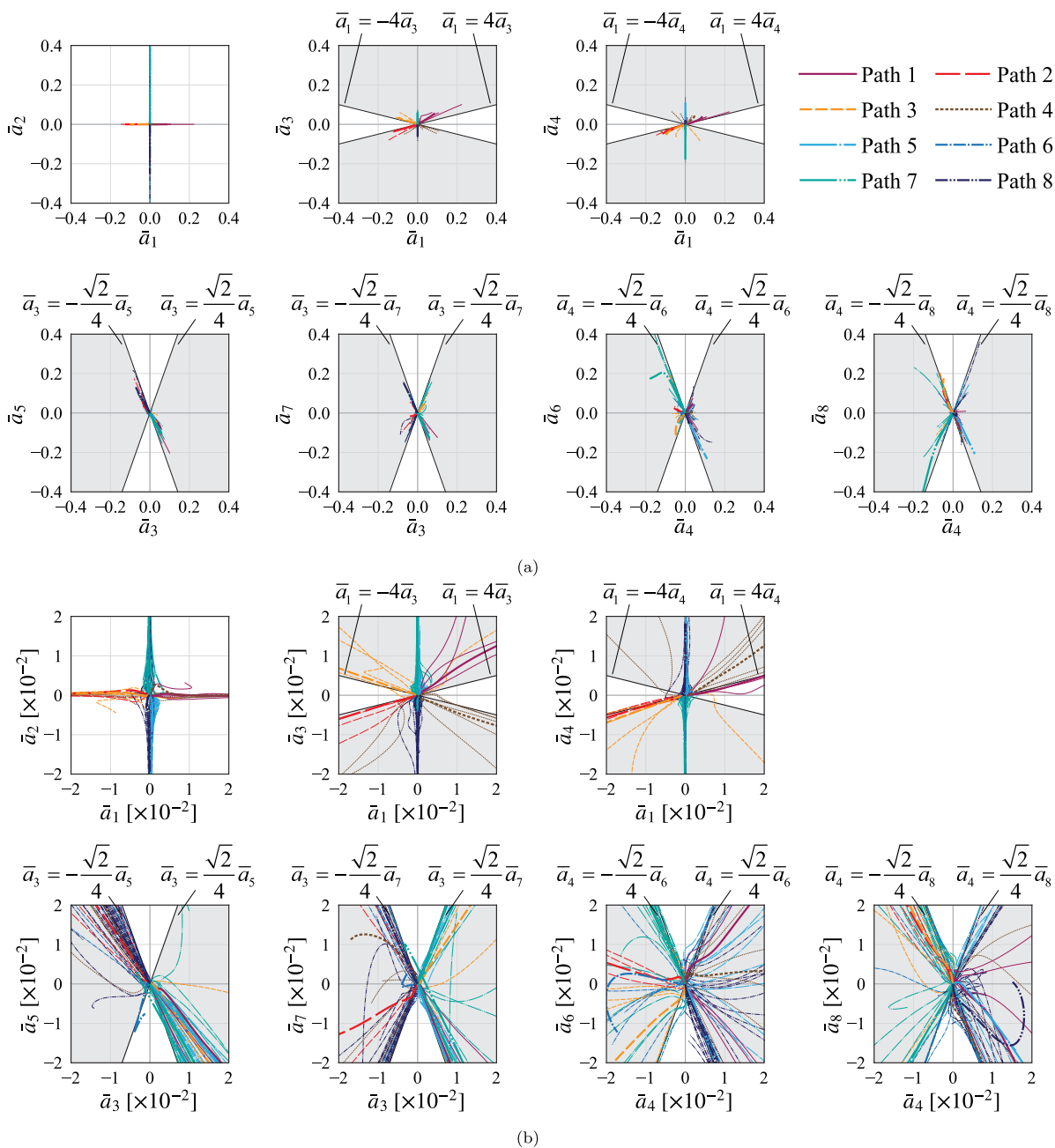


Fig. 19. Values of coefficients of infinitesimal mechanism modes $\bar{a}_1, \dots, \bar{a}_8$ on folding paths of DWC model: (a) overall view and (b) detailed view. The coefficients can exist in the gray regions.

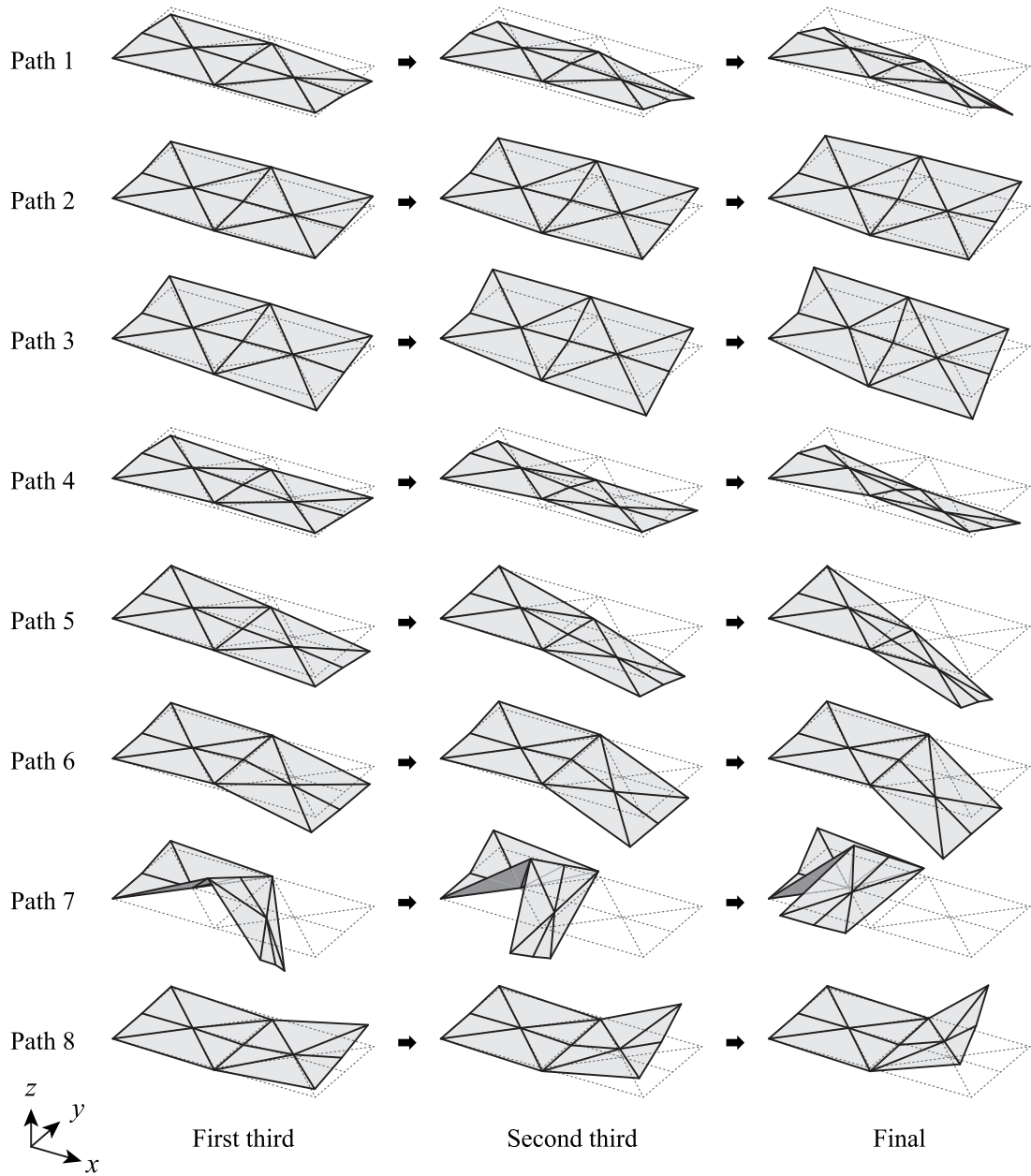


Fig. 20. Folding sequences obtained in large deformation analysis of DWC model corresponding to bold lines in Fig. 19. The first, second, and third columns are deformed shapes at the first third, second third, and end of folding path, respectively.

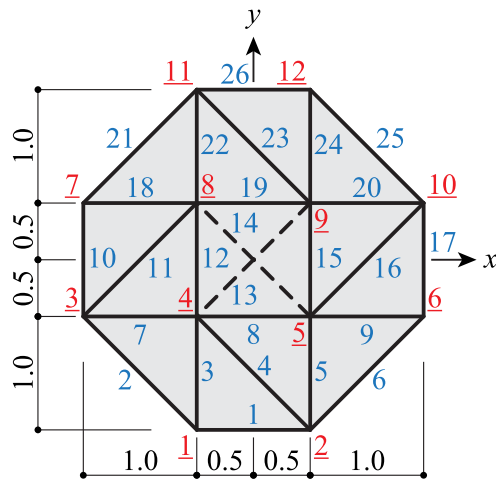


Fig. 21. Flasher pattern in the initial flat state. Node indices are written in red with underlines and bar indices are written in blue, and the bars of the truss model placed along the diagonals are represented by dashed lines. (For interpretation of the references to color in this figure legend, the reader is referred to the web version of this article.)

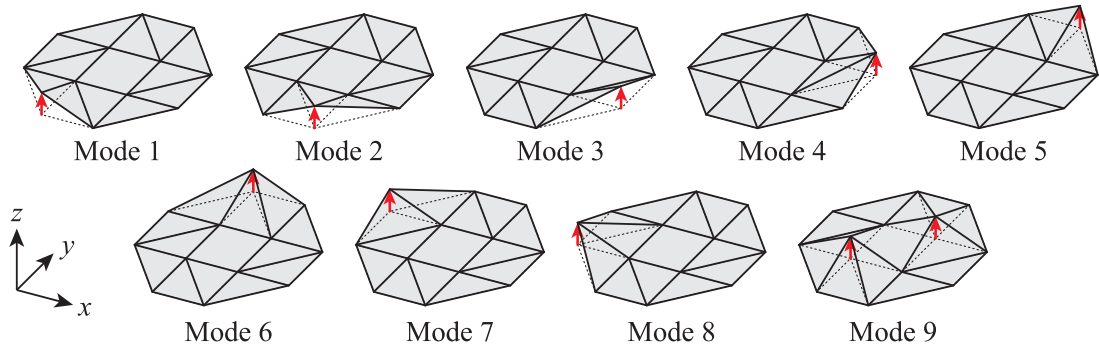


Fig. 22. Nodal displacements in non-trivial infinitesimal mechanism modes of flasher model. Vectors indicated by red arrows are unit vectors in the z-direction. In modes 1–8, only one node moves, and in mode 9, the quadrilateral face at the center is bent.

from the modes shown in Tables 6 and 7:

$$\begin{cases}
 4a_9^2 = 0 \\
 a_1^2 - 2a_1a_2 - 2a_1a_8 + 2a_1a_9 + a_2^2 + 2a_2a_9 \\
 \quad - 2a_4a_5 + 4a_4a_9 + a_5^2 - 2a_5a_6 + 2a_5a_9 + a_6^2 + 2a_6a_9 + 4a_8a_9 - 10a_9^2 = 0 \\
 -2a_2a_3 - 2a_2a_9 + a_3^2 - 2a_3a_4 + a_4^2 - 2a_4a_9 \\
 \quad - 2a_6a_7 - 2a_6a_9 + a_7^2 - 2a_7a_8 + a_8^2 - 2a_8a_9 + 2a_9^2 = 0 \\
 a_1^2 - 2a_1a_2 - 2a_1a_8 + 2a_1a_9 + a_2^2 + 2a_2a_9 \\
 \quad + 2a_4a_5 - 4a_4a_9 - a_5^2 + 2a_5a_6 - 2a_5a_9 - a_6^2 - 2a_6a_9 + 4a_8a_9 = 0 \\
 -2a_2a_3 - 2a_2a_9 + a_3^2 - 2a_3a_4 + a_4^2 - 2a_4a_9 \\
 \quad + 2a_6a_7 + 2a_6a_9 - a_7^2 + 2a_7a_8 - a_8^2 + 2a_8a_9 = 0
 \end{cases} \tag{49}$$

$$\Leftrightarrow \begin{cases}
 a_9 = 0 \\
 a_1^2 - 2(a_8 + a_2)a_1 + a_2^2 = 0 \\
 a_3^2 - 2(a_2 + a_4)a_3 + a_4^2 = 0 \\
 a_5^2 - 2(a_4 + a_6)a_5 + a_6^2 = 0 \\
 a_7^2 - 2(a_6 + a_8)a_7 + a_8^2 = 0.
 \end{cases}$$

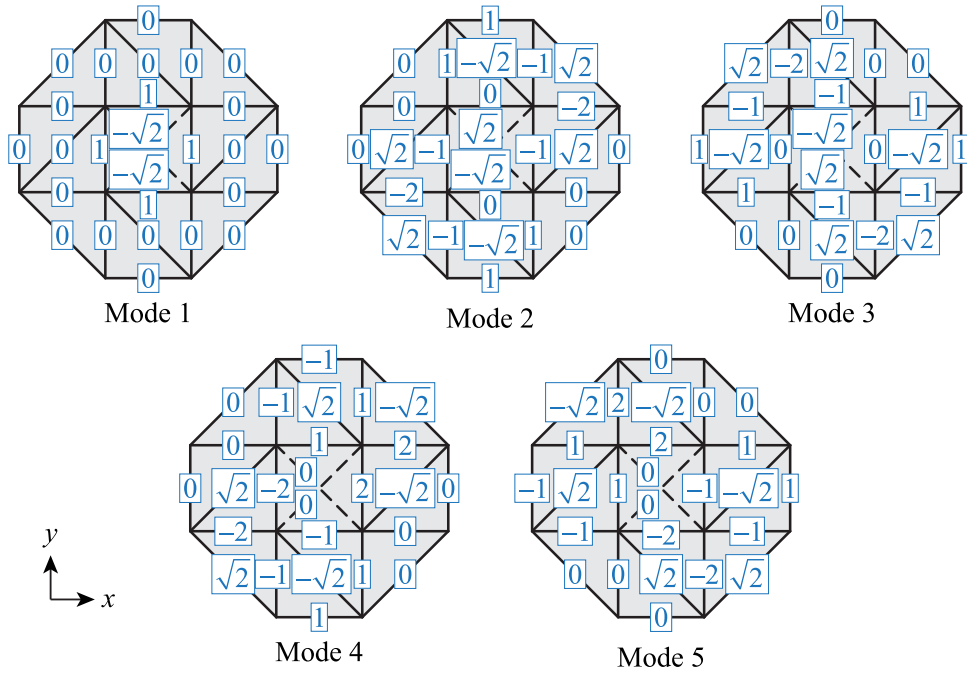


Fig. 23. Axial bar forces ω_i/l_i calculated from self-equilibrium force density modes of flasher model. Positive and negative values correspond to tension and compression forces, respectively.

The last four equations in Eq. (49) can be solved for $a_1, a_3, a_5,$ and a_7 if $a_2, a_4, a_6,$ and a_8 satisfy

$$\begin{cases} a_8(a_8 + 2a_2) \geq 0 \\ a_2(a_2 + 2a_4) \geq 0 \\ a_4(a_4 + 2a_6) \geq 0 \\ a_6(a_6 + 2a_8) \geq 0. \end{cases} \tag{50}$$

The left-hand sides of the inequalities in Eq. (50) are simultaneously equal to zero if and only if $a_2 = a_4 = a_6 = a_8 = 0$. Only in this case, $a_1, a_3, a_5,$ and a_7 have double roots, and $a_1 = a_3 = a_5 = a_7 = 0$ holds. Therefore, $a_2, a_4, a_6,$ and a_8 satisfying Eq. (50) can be treated as the independent coefficients, and the kinematic path of the flasher pattern in Fig. 21 bifurcates into $2^4 = 16$ distinct paths in the flat state $a_1 = \dots = a_8 = 0$ according to the sign combinations of the square root terms in the following four dependent coefficients:

$$\begin{cases} a_1 = a_8 + a_2 \pm \sqrt{a_8^2 + 2a_8a_2} \\ a_3 = a_2 + a_4 \pm \sqrt{a_2^2 + 2a_2a_4} \\ a_5 = a_4 + a_6 \pm \sqrt{a_4^2 + 2a_4a_6} \\ a_7 = a_6 + a_8 \pm \sqrt{a_6^2 + 2a_6a_8}. \end{cases} \tag{51}$$

6.3.2. Observation of results of infinitesimal mechanism analysis

The first equation in Eq. (49) implies that the infinitesimal mechanism mode in which the central quadrilateral face is bent disappear in the deformation where a finite mechanism may exist. The remaining four equations represents the relationship among the movement of the nodes on the perimeters. If $a_1, a_3, a_5,$ or a_7 equals to zero, their corresponding coefficients $a_2, a_4, a_6,$ or $a_8,$ respectively, also equals zero. Therefore, if node 1, 6, 12, or 7 stays in its initial position, their corresponding node 2, 10, 11, or 3, respectively, also does not move. On the other hand, if $a_2, a_4, a_6,$ or a_8 equals to zero, $(a_1, a_3) = (a_8 \pm |a_8|, a_4), (a_3, a_5) = (a_2 \pm |a_2|, a_6), (a_5, a_7) = (a_4 \pm |a_4|, a_8),$ or $(a_7, a_1) = (a_6 \pm |a_6|, a_2),$ respectively, is satisfied. This implies that if node 2, 10, 11, or 3 stays in its initial position, the relative motion of the two consecutive nodes next to that node is constrained. In addition, each of nodes 1, 6, 7, and 12 moves following one of the two adjacent nodes on the perimeters that moves greater than another because the signs of $a_1, a_3, a_5,$ and a_7 correspond to the signs of $a_8 + a_2, a_2 + a_4, a_4 + a_6,$ and $a_6 + a_8,$ respectively, from Eq. (51).

Table 8
Combinations of the sign of the square root terms in Eq. (51) for the classification of 16 bifurcation paths.

Term	1	2	3	4	5	6	7	8	9	10	11	12	13	14	15	16
$\sqrt{a_8^2 + 2a_8a_2}$	+	+	+	+	-	+	+	-	+	-	-	+	-	-	-	-
$\sqrt{a_2^2 + 2a_2a_4}$	+	+	+	-	+	+	-	+	-	+	-	-	+	-	-	-
$\sqrt{a_4^2 + 2a_4a_6}$	+	+	-	+	+	-	+	+	-	-	+	-	-	+	-	-
$\sqrt{a_6^2 + 2a_6a_8}$	+	-	+	+	+	-	-	-	+	+	+	-	-	-	+	-

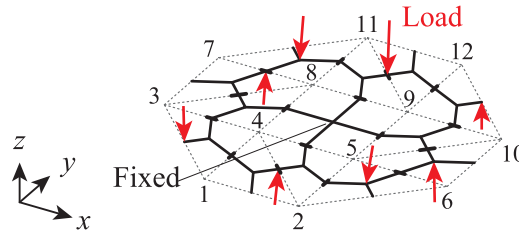


Fig. 24. Frame model of flasher model for large deformation analysis. Translation and rotation of the node on the quadrilateral face at the center are constrained, and nodal loads are applied to eight randomly selected nodes as indicated by red arrows. (For interpretation of the references to color in this figure legend, the reader is referred to the web version of this article.)

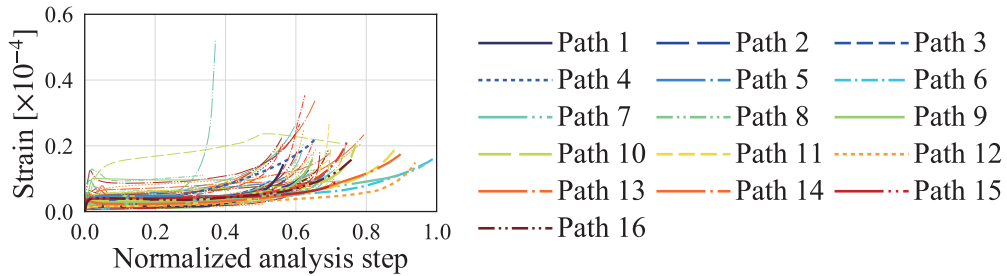


Fig. 25. Maximum absolute strain among edges along folding paths of flasher model. Strain values are small, and all the paths can be approximately regarded as rigid-folding paths.

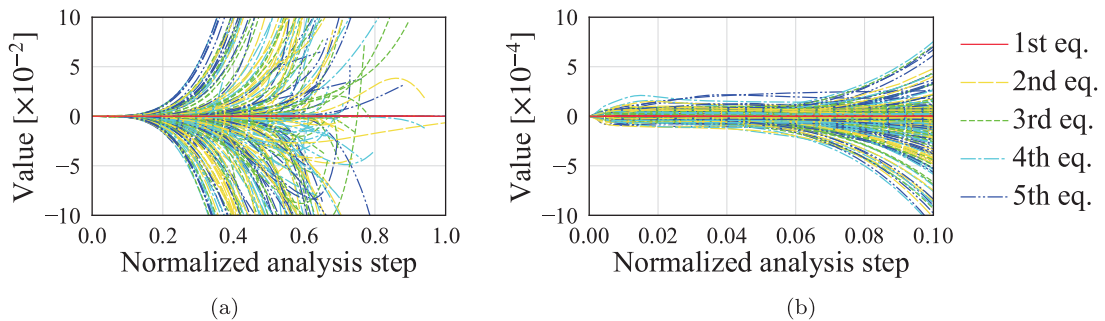


Fig. 26. Values of left-hand sides of Eq. (49) over a_1, \dots, a_9 , which are fairly small in the vicinity of the initial flat state: (a) overall view and (b) detailed view.

6.3.3. Comparison to large deformation analysis

The frame model for the large deformation analysis is shown in Fig. 24. The translation and rotation of the node on the face whose vertices are 4, 5, 8, and 9 are constrained to avoid rigid-body motion of the entire model. The nodal loads are applied to eight randomly selected nodes except for the nodes connected to the fixed node, and their magnitude and direction are randomly determined in the same manner as in Section 6.1.3. A hundred folding paths are obtained from the large deformation analysis, and they are classified into 16 bifurcation paths based on the sign of the square root terms in Eq. (51), as summarized in Table 8.

Figs. 25, 26, and 27 show the transition of the maximum absolute value of the edge strain, the value of the left-hand sides of the quadratic Eqs. (49), and the coefficients $a_1 \dots, a_8$ for several coefficient pairs, respectively. The value of a_9 is not plotted in Fig. 27

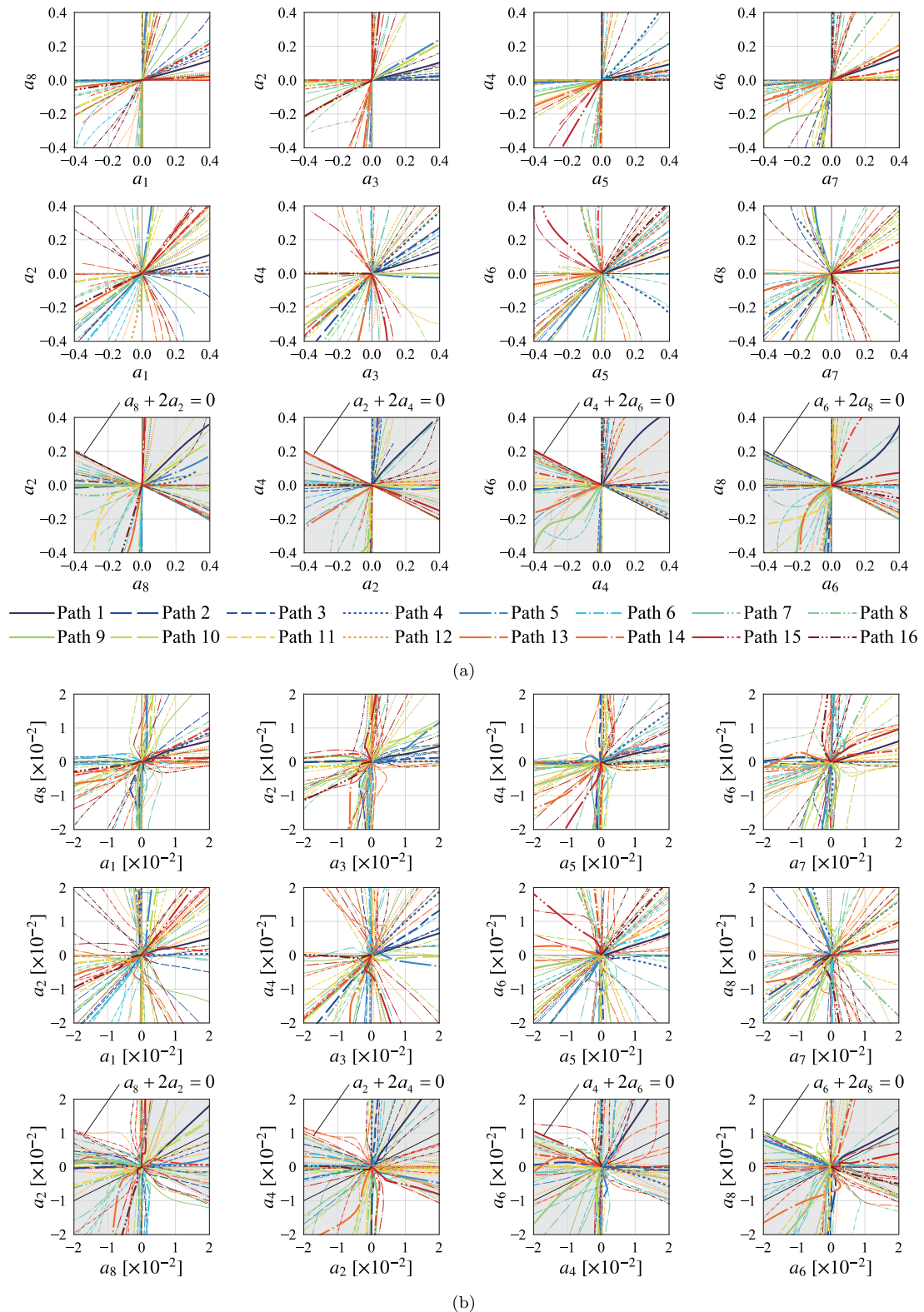


Fig. 27. Values of a_1, \dots, a_9 on folding paths of flasher model: (a) overall view and (b) detailed view. The coefficients can exist in gray regions in the third and sixth rows.

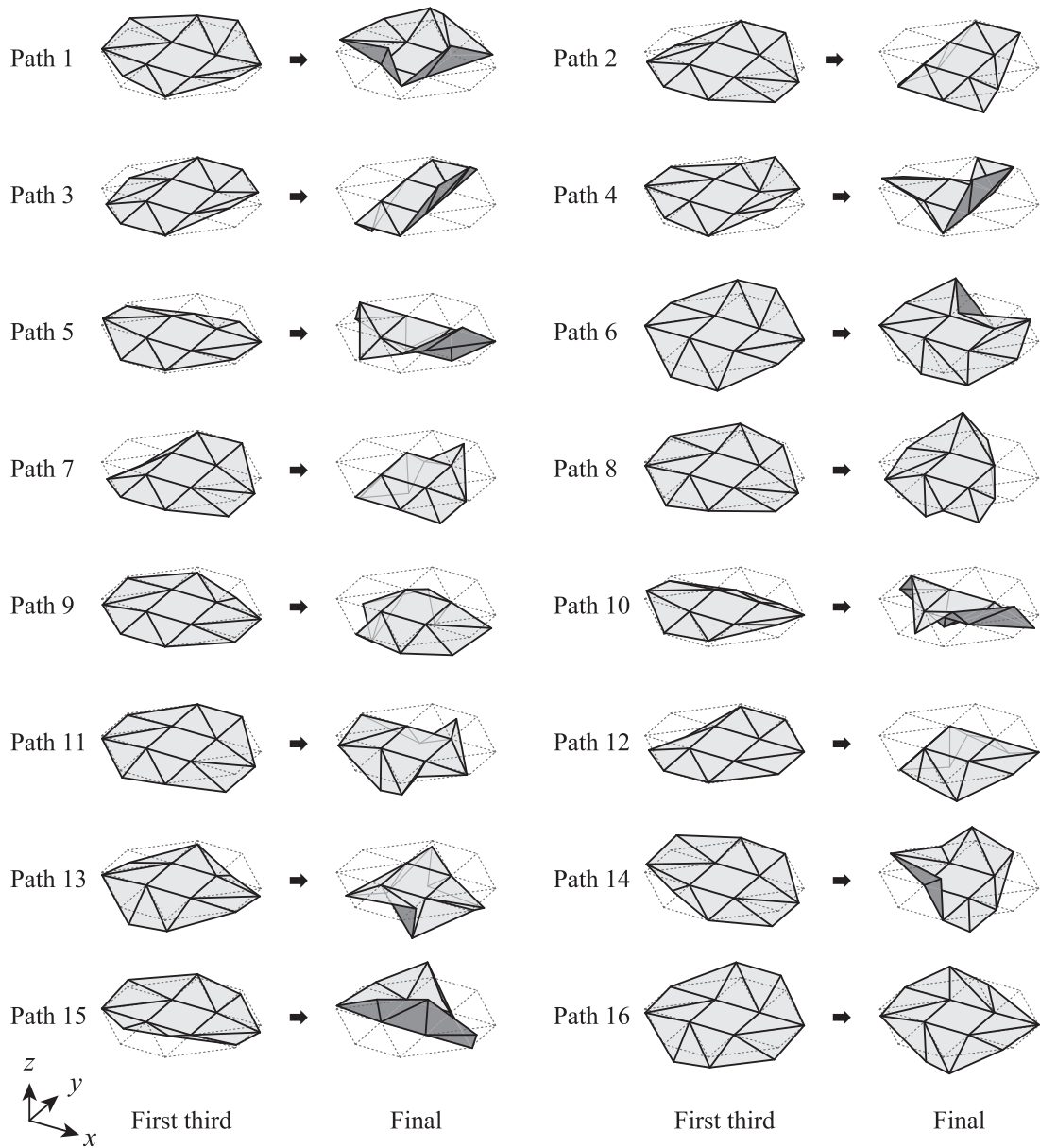


Fig. 28. Folding sequences obtained in large deformation analysis of flasher model corresponding to bold lines in Fig. 27. The first and third columns are deformed shapes at the first third of folding path, and the second and fourth columns are deformed shapes at the end of folding path.

because it is approximately equal to zero, as indicated by red lines in Fig. 26. The folding processes on the obtained paths indicated by the bold lines in Figs. 25 and 27 are shown in Fig. 28. The 16 line types in Figs. 25 and 27 represent the classification of the obtained path listed in Table 8.

As shown in Figs. 25 and 26, the obtained paths are approximately rigid-folding paths, and the quadratic Eqs. (49) are well satisfied when the deformation is small. The gray hatched regions in the third and sixth rows in Fig. 27 represent the regions where the square root terms in Eq. (51) are real, and most paths are within the indicated gray regions. In addition, we can see from Fig. 25 that the signs of a_1 , a_3 , a_5 , and a_7 are the same as the signs of a_8 , a_2 , a_4 , and a_6 , respectively.

7. Discussion and conclusions

In this article, second-order infinitesimal mechanisms and bifurcation paths of rigid origami are investigated by using truss models. Combinations of the infinitesimal mechanism modes of the truss model that satisfy the existence conditions of second-order infinitesimal mechanisms are investigated for three simple crease patterns, and the results of the infinitesimal mechanism

analysis are compared to the finite mechanisms obtained in the large deformation analysis of frame models. The conditions for the existence of a second-order infinitesimal mechanism are formulated as quadratic equations with respect to the coefficients of the infinitesimal mechanism modes, and they are analytically solved to obtain the entire system of solutions. From the observations of the quadratic equations and their solutions, several distinct features were found: the bifurcations of the deformation paths, the disappeared combinations of the mechanism modes in a single path, and the local properties related to the distribution of the self-equilibrium axial forces and the nodal displacement. As shown for the Miura-based model and the flasher model, the infinitesimal mechanism modes in which the quadrilateral faces are bent do not appear in the potential finite mechanisms if the second-order infinitesimal mechanisms are considered. These observations are consistent with the results in the large deformation analysis. The results of the large deformation analysis also showed that, for multi-degree-of-freedom mechanisms, the coefficients of the infinitesimal mechanism modes are non-uniformly distributed over the regions where a second-order infinitesimal mechanism exists. This non-uniform path distribution may be due to the stiffness distribution of the model in the large deformation analysis. Furthermore, third- or higher-order infinitesimal mechanism may explain this path distribution. However, this cannot be concluded only from the results obtained in this study, and further investigation is needed.

For general complex crease patterns, it is very difficult to solve a system of quadratic equations for the existence of second-order infinitesimal mechanisms analytically and to evaluate the solution qualitatively. Thus, the equations are not solved manually. Packages for solving a system of quadratic equations by symbolic computation are available in some mathematical processing software packages, and it is theoretically possible to solve the equations with some limitations (see Ref. [26]). Moreover, it is relatively easy to obtain partial solutions by using a numerical solution method. Therefore, the issue in analyzing bifurcation paths using the existence conditions of second-order infinitesimal mechanisms is not the solution method of the system of quadratic equations itself, but the determination of infinitesimal deformation modes and self-equilibrium force density modes to obtain a solution that is easy to interpret physically and geometrically. For example, these modes can be obtained by the singular value decomposition of the compatibility matrix [26], but the interpretation of the solution is often difficult when the modes are obtained in this manner. Although no framework for determining these modes has been established, we list two possible directions below.

One possible direction is to determine the modes based on the local properties. As observed in the examples, the relation between the self-equilibrium force density mode and the infinitesimal mechanism mode is strong, and these modes have a common local distribution in the quadratic equation for the existence of a second-order infinitesimal mechanism. This local property may help simplify the equations, as demonstrated in the derivation of Eq. (45). Therefore, by setting up self-equilibrium force density modes and infinitesimal mechanism modes to have a common local distribution, we may obtain a system of equations that produces solutions that are easy to derive and interpret.

Another direction is to determine the modes based on the symmetry condition. If a mechanism and a self-equilibrium state have symmetric structures, a group theoretic approach can be applied to obtain a finite mechanism [12,14]. Ref. [12] states that a mechanism that belongs to a nondegenerate representation of a symmetry group is finite if there is neither a self-equilibrium state that has the same symmetry condition with the mechanism nor a totally symmetric self-equilibrium state. This indicates that the quadratic equation for the existence of a second-order infinitesimal mechanism may be simplified by considering the symmetry conditions in self-equilibrium force density modes and infinitesimal mechanism modes.

As discussed above, considering higher-order infinitesimal mechanisms allows the direction of deformation in which a finite mechanism may exist to be significantly limited without carrying out large deformation analysis, and it is possible to analyze branching paths efficiently. While there is still much work to be done, this study will help to establish a systematic method to analyze higher-order mechanisms and branching paths of rigid origami.

Declaration of competing interest

The authors declare that they have no known competing financial interests or personal relationships that could have appeared to influence the work reported in this paper.

Data availability

Data will be made available on reasonable request.

Acknowledgments

This work was supported by the Japan Science and Technology Agency, CREST Grant Number JPMJCR1911 and the JSPS, Japan KAKENHI Grant Number JP23K19160.

References

- [1] S.A. Zirbel, R.J. Lang, M.W. Thomson, D.A. Sigel, P.E. Walkemeyer, B.P. Trease, S.P. Magleby, L.L. Howell, Accommodating thickness in origami-based deployable arrays, *J. Mech. Des.* 135 (11) (2013) 111005, <http://dx.doi.org/10.1115/1.4025372>.
- [2] J. Morgan, S.P. Magleby, L.L. Howell, An approach to designing origami-adapted aerospace mechanisms, *J. Mech. Des.* 138 (5) (2016) 052301, <http://dx.doi.org/10.1115/1.4032973>.
- [3] K. Kuribayashi, K. Tsuchiya, Z. You, D. Tomus, M. Umemoto, T. Ito, M. Sasaki, Self-deployable origami stent grafts as a biomedical application of Ni-rich TiNi shape memory alloy foil, *Mater. Sci. Eng. A* 419 (1) (2006) 131–137, <http://dx.doi.org/10.1016/j.msea.2005.12.016>.

- [4] B. An, S. Miyashita, A. Ong, M.T. Tolley, M.L. Demaine, E.D. Demaine, R.J. Wood, D. Rus, An end-to-end approach to self-folding origami structures, *IEEE Trans. Robot.* 34 (6) (2018) 1409–1424, <http://dx.doi.org/10.1109/TRO.2018.2862882>.
- [5] C.H. Belke, J. Paik, Mori: A modular origami robot, *IEEE/ASME Trans. Mechatronics* 22 (5) (2017) 2153–2164, <http://dx.doi.org/10.1109/TMECH.2017.2697310>.
- [6] J.L. Silverberg, A.A. Evans, L. McLeod, R.C. Hayward, T. Hull, C.D. Santangelo, I. Cohen, Applied origami. Using origami design principles to fold reprogrammable mechanical metamaterials, *Science* 345 (6197) (2014) 647–650, <http://dx.doi.org/10.1126/science.1252876>.
- [7] E.T. Filipov, T. Tachi, G.H. Paulino, Origami tubes assembled into stiff, yet reconfigurable structures and metamaterials, *Proc. Natl. Acad. Sci.* 112 (40) (2015) 12321–12326, <http://dx.doi.org/10.1073/pnas.1509465112>.
- [8] A. Karanouh, E. Kerber, Innovations in dynamic architecture, *J. Facade Des. Eng.* 3 (2) (2015) 185–221, <http://dx.doi.org/10.3233/FDE-150040>.
- [9] T. Lee, J.M. Gattas, Geometric design and construction of structurally stabilized accordion shelters, *J. Mech. Robotics* 8 (3) (2016) 031009–1–031009–8, <http://dx.doi.org/10.1115/1.4032441>.
- [10] J. Farnham, T.C. Hull, A. Rumbolt, Rigid folding equations of degree-6 origami vertices, *Proc. R. Soc. A: Math., Phys. Eng. Sci.* 478 (2260) (2022) 20220051, <http://dx.doi.org/10.1098/rspa.2022.0051>.
- [11] Y. Wang, Q. Zhang, X. Zhang, J. Cai, C. Jiang, Y. Xu, J. Feng, Analytical and numerical analysis of mobility and kinematic bifurcation of planar linkages, *Int. J. Non-Linear Mech.* 145 (2022) 104110, <http://dx.doi.org/10.1016/j.ijnonlinmec.2022.104110>.
- [12] S.D. Guest, P.W. Fowler, Symmetry conditions and finite mechanisms, *J. Mech. Mater. Struct.* 2 (2) (2007) 293–301, <http://dx.doi.org/10.2140/jomms.2007.2.293>.
- [13] T. Tachi, Generalization of rigid foldable quadrilateral mesh origami, in: A. Domingo, C. Lázaro (Eds.), *Proceedings of the International Association for Shell and Spatial Structures (IASS) Annual Symposium 2009*, Valencia, Spain, 2009.
- [14] R. Watada, M. Ohsaki, Y. Kanno, Group theoretic approach to large-deformation property of three-dimensional bar-hinge mechanism, *Japan J. Ind. Appl. Math.* 36 (2018) 177–208, <http://dx.doi.org/10.1007/s13160-018-0336-6>.
- [15] T. Tachi, Simulation of rigid origami, in: R.J. Lang (Ed.), *Proceedings of the 4th International Meeting of Origami Science, Mathematics, and Education*, (Origami4), AK Peters, Natick, MA, United States of America, 2009, pp. 175–187.
- [16] K. Liu, G.H. Paulino, Highly efficient nonlinear structural analysis of origami assemblages using the MERLIN2 software, in: R.J. Lang, M. Bolitho, Z. You (Eds.), *Proceedings of the 7th International Meeting of Origami Science, Mathematics, and Education*, (Origami7), Tarquin, St Albans, United Kingdom, 2018, 1197–1182.
- [17] A. Ghassaei, E.D. Demaine, N. Gershenfeld, Fast, interactive origami simulation using GPU computation, in: R.J. Lang, M. Bolitho, Z. You (Eds.), *Proceedings of the 7th International Meeting of Origami Science, Mathematics, and Education*, (Origami7), Tarquin, St Albans, United Kingdom, 2018, pp. 1151–1156.
- [18] M. Schenk, S.D. Guest, Origami folding: A structural engineering approach, in: P. Wang-Iverson, R.J. Lang, M. Yim (Eds.), *Proceedings of the 5th International Meeting of Origami Science, Mathematics, and Education*, (Origami5), CRC Press, 2011, pp. 291–303.
- [19] S. Pellegrino, C.C. R., Matrix analysis of statically and kinematically indeterminate frameworks, *Int. J. Solids Struct.* 22 (4) (1986) 409–428, [http://dx.doi.org/10.1016/0020-7683\(86\)90014-4](http://dx.doi.org/10.1016/0020-7683(86)90014-4).
- [20] E.N. Kuznetsov, Underconstrained structural systems, *Int. J. Solids Struct.* 24 (2) (1988) 153–163, [http://dx.doi.org/10.1016/0020-7683\(88\)90026-1](http://dx.doi.org/10.1016/0020-7683(88)90026-1).
- [21] T. Tarnai, Higher-order infinitesimal mechanisms, *Acta Tech. Acad. Sci. Hung.* 102 (3–4) (1989) 363–378.
- [22] N. Vassart, R. Laporte, R. Motro, Determination of mechanisms order for kinematically and statically indetermined systems, *Int. J. Solids Struct.* 37 (28) (2000) 3807–3839, [http://dx.doi.org/10.1016/S0020-7683\(99\)00178-X](http://dx.doi.org/10.1016/S0020-7683(99)00178-X).
- [23] N. Watanabe, K. Kawaguchi, The method for judging rigid foldability, in: R.J. Lang (Ed.), *Proceedings of the 4th International Meeting of Origami Science, Mathematics, and Education*, (Origami4), AK Peters, 2009, pp. 165–174.
- [24] T. Tachi, Design of infinitesimally and finitely flexible origami based on reciprocal figures, *J. Geom. Graph.* 16 (2) (2012) 223–234.
- [25] E.D. Demaine, M.D. Demaine, D.A. Huffman, T.C. Hull, D. Koschitz, T. Tachi, Zero-area reciprocal diagram of origami, in: *Proceedings of the International Association for Shell and Spatial Structures (IASS) Annual Symposium 2016*, Tokyo, Japan, 2016.
- [26] P. Kumar, S. Pellegrino, Computation of kinematic paths and bifurcation points, *Int. J. Solids Struct.* 37 (46) (2000) 7003–7027, [http://dx.doi.org/10.1016/S0020-7683\(99\)00327-3](http://dx.doi.org/10.1016/S0020-7683(99)00327-3).
- [27] B.G. Chen, C.D. Santangelo, Branches of triangulated origami near the unfolded state, *Phys. Rev. X* 8 (2018) 011034, <http://dx.doi.org/10.1103/PhysRevX.8.011034>.
- [28] J. Cai, Q. Zhong, X. Zhang, K. Wang, Q. Zhang, J. Feng, Mobility and kinematic bifurcation analysis of origami plate structures, *J. Mech. Robotics* 15 (6) (2023) 061015, <http://dx.doi.org/10.1115/1.4056576>.
- [29] M.J. Sewell, A general theory of equilibrium paths through critical points. I, *Proc. R. Soc. London Ser. A Math. Phys. Sci.* 306 (1485) (1968) 201–223, <http://dx.doi.org/10.1098/rspa.1968.0146>.
- [30] M.J. Sewell, A general theory of equilibrium paths through critical points. II, *Proc. R. Soc. London Ser. A Math. Phys. Sci.* 306 (1485) (1968) 225–238, <http://dx.doi.org/10.1098/rspa.1968.0147>.
- [31] K.C. Johns, A.H. Chilver, Multiple path generation at coincident branching points, *Int. J. Mech. Sci.* 13 (11) (1971) 899–910, [http://dx.doi.org/10.1016/0020-7403\(71\)90076-2](http://dx.doi.org/10.1016/0020-7403(71)90076-2).
- [32] K.C. Johns, Simultaneous buckling in symmetric structural systems, *J. Eng. Mech. Div.* 98 (4) (1972) 835–848, <http://dx.doi.org/10.1061/JMCEA3.0001641>.
- [33] A. Magnusson, Analysis of post-buckling branches at multiple symmetric bifurcations, *Internat. J. Numer. Methods Eng.* 51 (4) (2001) 413–428, <http://dx.doi.org/10.1002/nme.157>.
- [34] M. Ohsaki, K. Ikeda, Imperfection sensitivity analysis of hill-top branching with many symmetric bifurcation points, *Int. J. Solids Struct.* 43 (16) (2006) 4704–4719, <http://dx.doi.org/10.1016/j.ijsolstr.2005.06.036>.
- [35] E.T. Filipov, K. Liu, T. Tachi, M. Schenk, G.H. Paulino, Bar and hinge models for scalable analysis of origami, *Int. J. Solids Struct.* 124 (2017) 26–45, <http://dx.doi.org/10.1016/j.ijsolstr.2017.05.028>.
- [36] T. Zhang, K. Kawaguchi, M. Wu, A folding analysis method for origami based on the frame with kinematic indeterminacy, *Int. J. Mech. Sci.* 146–147 (2018) 234–248, <http://dx.doi.org/10.1016/j.ijmecsci.2018.07.036>.
- [37] R. Wang, Y. Song, J.S. Dai, Reconfigurability of the origami-inspired integrated 8R kinematotropic metamorphic mechanism and its evolved 6R and 4R mechanisms, *Mech. Mach. Theory* 161 (2021) 104245, <http://dx.doi.org/10.1016/j.mechmachtheory.2021.104245>.
- [38] K. Hayakawa, M. Ohsaki, Form generation of rigid origami for approximation of a curved surface based on mechanical property of partially rigid frames, *Int. J. Solids Struct.* 216 (2021) 182–199, <http://dx.doi.org/10.1016/j.ijsolstr.2020.12.007>.
- [39] K. Hayakawa, M. Ohsaki, Equilibrium path and stability analysis of rigid origami using energy minimization of frame model, *Front. Built Environ.* 8 (2022) <http://dx.doi.org/10.3389/fbuil.2022.995710>.
- [40] R. Connelly, W. Whiteley, Second-order rigidity and prestress stability for tensegrity frameworks, *SIAM J. Discrete Math.* 9 (3) (1996) 453–491, <http://dx.doi.org/10.1137/S0895480192229236>.
- [41] R. Watada, M. Ohsaki, Series expansion method for determination of order of 3-dimensional bar-joint mechanism with arbitrarily inclined hinges, *Int. J. Solids Struct.* 141–142 (2018) 78–85, <http://dx.doi.org/10.1016/j.ijsolstr.2018.02.012>.
- [42] Z. He, S.D. Guest, On rigid origami III: local rigidity analysis, *Proc. R. Soc. Lond. Ser. A Math. Phys. Eng. Sci.* 478 (2258) (2022) 20210589, <http://dx.doi.org/10.1098/rspa.2021.0589>.
- [43] C.D. Meyer, *Matrix Analysis and Applied Linear Algebra*, SIAM, Philadelphia, PA, United States of America, 2000.
- [44] J. Zhang, M. Ohsaki, Adaptive force density method for form-finding problem of tensegrity structures, *Int. J. Solids Struct.* 43 (18) (2006) 5658–5673, <http://dx.doi.org/10.1016/j.ijsolstr.2005.10.011>.
- [45] Dassault Systèmes Simulia Corp., *Abaqus 2022 documentation*, 2022.